Advanced topics on rotor blade full-scale structural fatigue testing and requirements

Berring, Peter; Fedorov, Vladimir; Belloni, Federico; Branner, Kim

Publication date:
2014

Document Version
Publisher's PDF, also known as Version of record

Advanced topics on rotor blade full-scale structural fatigue testing and requirements

Department of Wind Energy E Report 2015

Peter Berring, Vladimir Fedorov, Federico Belloni & Kim Branner

DTU Wind Energy E-0068

ISBN: 978-87-93278-10-3

December 2014

DTU Wind Energy
Department of Wind Energy

Authors: Peter Berring, Vladimir Fedorov, Federico Belloni & Kim Branner

Title: Advanced topics on rotor blade full-scale structural fatigue testing and requirements

Department: Department of Wind Energy

Summary (max 2000 characters):

Full scale fatigue test is an important part of the development and design of wind turbine blades. Testing is also needed for the approval of the blades in order for them to be used on large wind turbines. Fatigue test of wind turbine blades was started in the beginning of the 1980s and has been further developed since then. Structures in composite materials are generally difficult and time consuming to test for fatigue resistance. Therefore, several methods for testing of blades have been developed and exist today. Those methods are presented in [1].

This report deals with more advanced topics for fatigue testing of wind turbine blades. One challenge is how to fatigue test blades under realistic conditions. In order to study this topic a finite element based multibody formulation using the floating frame of reference approach is used to study fatigue loading under different external conditions.

An important purpose of full scale testing is to give valuable information to the designers on how the blade behaves in the test situation and which structural details that are important and should be included in the structural models for design. In order to be able to see the blade behaviour advanced measuring methods are needed.

DTU Wind Energy E-0068

December 2014

Contract no.:

104.Kina.1.MFS.4-1-2-5

Project no.:

Sponsorship:

Sino-Danish Renewable Energy Development (RED) Programme

Front page:

Pages: 50

Tables: 6

References: 8

Technical University of Denmark
Department of Wind Energy
Frederiksborgvej 399
Building 118
4000 Roskilde
Denmark
Telephone 46775470

kibr@dtu.dk
www.vindenergi.dtu.dk

Preface

This report is deliverable 1.1 part B of the project “Wind turbine rotor blade testing technology research and platform construction”. The project is supported by the Renewable Energy Development (RED) programme in which the Chinese and Danish governments are cooperating and aiming at institutional capacity building and technology innovation for renewable energy development.

This particular project is a partnership between the Chinese Baoding Diangu Renewable Energy Testing and Research Co., Ltd., a national wind and solar energy key laboratory for simulation and certification and from Denmark, the Department of Wind Energy, Technical University of Denmark, a Danish wind energy research department that has provided a major part of the wind energy research in Denmark and is one of the leading wind energy research institutions in the world.

The project will focus on research for on-site, full-scale and down-scale structural testing of wind turbine rotor blades. An advanced blade on-site monitoring platform and full-scale testing platform will be constructed to strengthen the capacity of wind turbine blade testing and demonstrated in Baoding, city of Hebei Province in China.

The project will provide the manufacturers with the possibility to do comprehensive blade testing in order to achieve test data for fulfilling requirements of standards and in order to obtain better and more optimized blade design. Meanwhile, advanced experiment tool and valid test data can also be provided for the research and certification institutions in order to develop better design methods and certification guidelines and standards.

The project has three main parts. The first part is research in full-scale and down-scale structural testing of wind turbine blades as well as condition monitoring for on-site testing of whole wind turbines. The next part is construction of platforms in China for full-scale fatigue testing of blades and on-site condition monitoring of wind turbines. Finally, the last part is to demonstrate the full-scale fatigue testing and the on-site condition monitoring.

Roskilde, Denmark
December 2014

Content

Summary

Full scale fatigue test is an important part of the development and design of wind turbine blades. Testing is also needed for the approval of the blades in order for them to be used on large wind turbines. Fatigue test of wind turbine blades was started in the beginning of the 1980s and has been further developed since then. Structures in composite materials are generally difficult and time consuming to test for fatigue resistance. Therefore, several methods for testing of blades have been developed and exist today. Those methods are presented in [1].

This report deals with more advanced topics for fatigue testing of wind turbine blades. One challenge is how to fatigue test blades under realistic conditions. In order to study this topic a finite element based multibody formulation using the floating frame of reference approach is used to study fatigue loading under different external conditions.

An important purpose of full scale testing is to give valuable information to the designers on how the blade behaves in the test situation and which structural details that are important and should be included in the structural models for design. In order to be able to see the blade behavior advanced measuring methods are needed.

1. Introduction

This report deals with more advanced topics for fatigue testing of wind turbine blades. It is abundantly clear that understanding of crack growth under ultimate loads serves as a basis to identify and understand those parameters that are also responsible for fatigue crack growth. Moreover, catastrophic failure can be triggered by cracks that have been initiated by fatigue growth until they reach a critical size. Catastrophic failure of wind turbine blades, due to excessive loading or fatigue damage, can lead to the destruction of the entire wind turbine. Structural failure of wind turbines not only causes a significant economic loss, but also poses a health and safety risk for people and facilities hit by parts that detach from the turbine and get airborne. It is therefore important to ensure that the blades can endure the loading they are exposed to throughout their lifetime. Full-scale tests represent an indispensable method to investigate all possible kinds of damage and damage mechanisms as a complimentary part of computationally based analysis methods. Moreover, full scale tests are considered as being close to scenarios a blade would experience in operational conditions. This means that full scale tests should give realistic failure mechanisms considering size effects and complex geometry as well as anisotropic material behavior.

It is also important to subject the blades to loads which represent, as close as possible, the loading that these wind turbine components will encounter during their lifetime. In order to study this topic a finite element based multibody formulation using the floating frame of reference approach is used to study fatigue loading under different external conditions.

An important purpose of full scale testing is to give valuable information to the designers on how the blade behaves in the test situation and which structural details that are important and should be included in the structural models for design. In order to be able to see the blade behavior advanced measuring methods are needed.

2. Fatigue loads on wind turbine blades

2.1 A Study of fatigue loads for a 2.05MW wind turbine

In this study the results from Seabra [2], are utilized to obtain some insight into the fatigue loads which this particular size of turbine blades are subjected to. Seabra [2] contains results of the load calculations of the wind turbine NM-80 (2.05MW) using SSP 34m blades with the aeroelastic program HAWC2 (v11.5). This code is a finite element based multibody formulation using the floating frame of reference approach. The turbine is pitch regulated with a variable speed generator. The control regulations are implemented as a separate module (Dynamic Link Library).

The wind conditions for the wind turbine is class IIB (V_{ave} = 8.5m/s, I_{ref} = 0.14). The wind shear was modelled using the power law model with an α = 0.2 and the turbulence was modelled with Mann model with a length scale of 29.4m. The fatigue loads were computed based on the IEC specified Design Load Cases (DLC), see Table 1. The lifetime equivalent loads are also

calculated based on a life time period of 20 years and using a Weibull distribution with the following parameters C = 9.6 and k = 2.

Table 1: Load cases used in fatigue load calculation

Design situation	DLC	Type of analysis	Yaw error [deg]	Prob. of occurrence in the LFT period [%]
Power Production	1.2	Fatigue	+/-10°	95
Power Production plus occurrence of a fault	2.4	Fatigue	+/-20°	2
Normal Shut down	4.1	Fatigue	--	2
Parked (standing still or idling)	6.4	Fatigue	--	1

Table 2: Weibull distribution of hours, normal load cases

WSP [m/s]	Hour distribution [h]
5	28769
7	31086
9	28296
11	22460
13	15812
15	9969
17	5663
19	2910
21	1356
23	575
25	222

2.2 Observations for the DLC 1.2 load case

In the following paragraph the load data from the Design Load Case 1.2 (Power Production) are utilized to evaluate the fatigue load characteristic for this particular wind turbine. Load case 2.4, 4.1 and 6.4 in Table 1 is not considered as the Life Fatigue Time (LFT) period for these load cases only adds up to 5%.

2.2.1 Loads at radial position R = 0m and R = 16m

From 5 m/s up to 13 m/s the load cloud, at radial position R = 0m, moves towards higher flap-wise (PTS) and higher edge-wise loading (TTL) . The flap-wise and edge-wise amplitude does not change significantly from 5 m/s to 11 m/s but at 13 m/s the turbine starts pitching which combined with the higher wind speeds has a significant effect on the load pattern. From 13 m/s up to 25 m/s the load cloud changes its shape as the flap-wise loads becomes more scattered. The flap-wise loads oscillate from negative to positive moments resulting in high amplitudes.

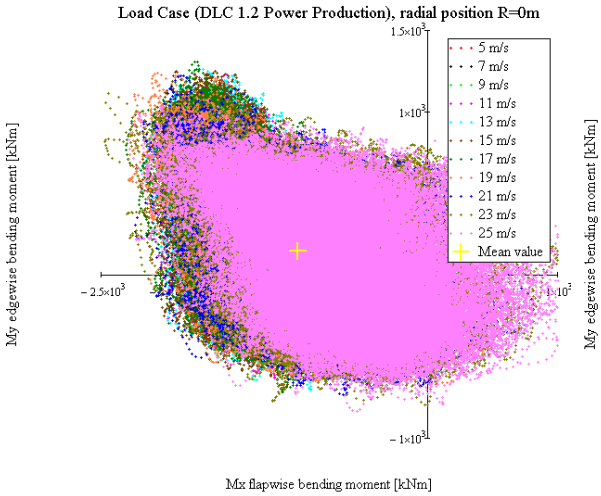

Figure 1: Complete load cloud at the root section

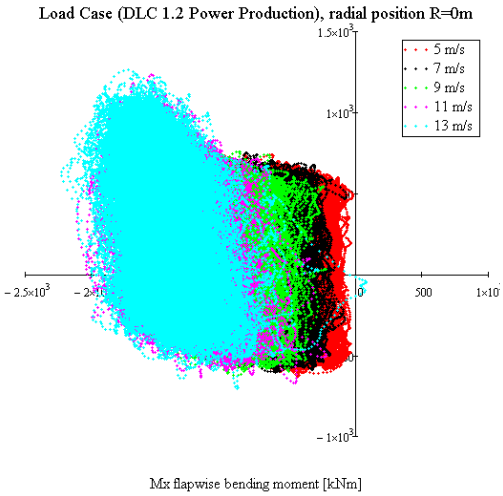

Figure 2: Load cloud for 5m/s….13m/s at the root section

The distribution between flap-wise and edgewise loading at radial position R = 16m is very similar to the shape of the load cloud at the root section (R = 0m). The loading at cross section 16m is approximately half of the loading at the root section.

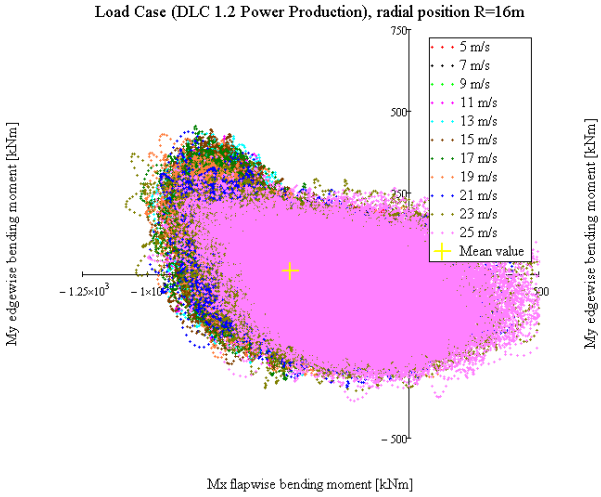

Figure 3: Complete load cloud at the cross section 16m

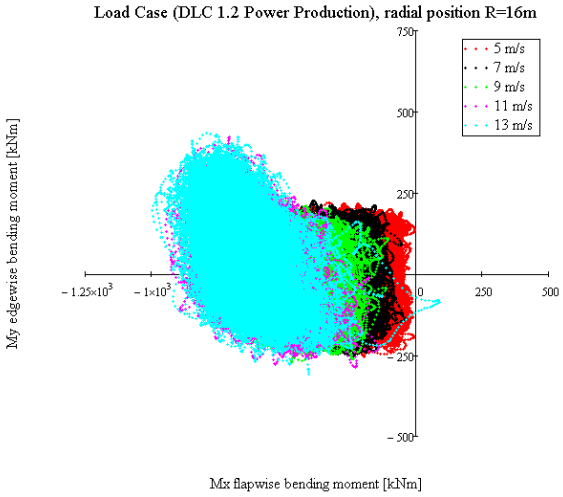

Figure 4: Load cloud for 5m/s…13m/s at the cross section 16m

By plotting the mean value of the flap-wise and edge-wise loading for the different wind speed steps it becomes clear how the load cloud moves at different wind speeds. For both cross sections the maximum mean values are found at 13 m/s. The path up (from 5m/s to 13 m/s) is very similar to the path down (from 13 m/s to 25 m/s). For the cross section at radial position 16meter the edge-wise loading changes sign.

In Figure 5 and Figure 6 the mean value for the entire load case DLC 1.2 is also plotted. This mean value is computed based on the hour distribution at the different wind speed steps. This point is mean value of the entire DLC 1.2.

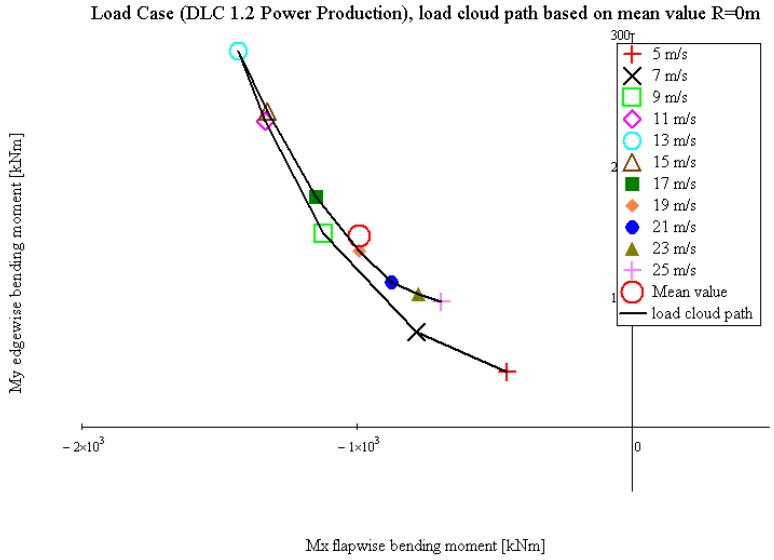

Figure 5: Load cloud path at the root section

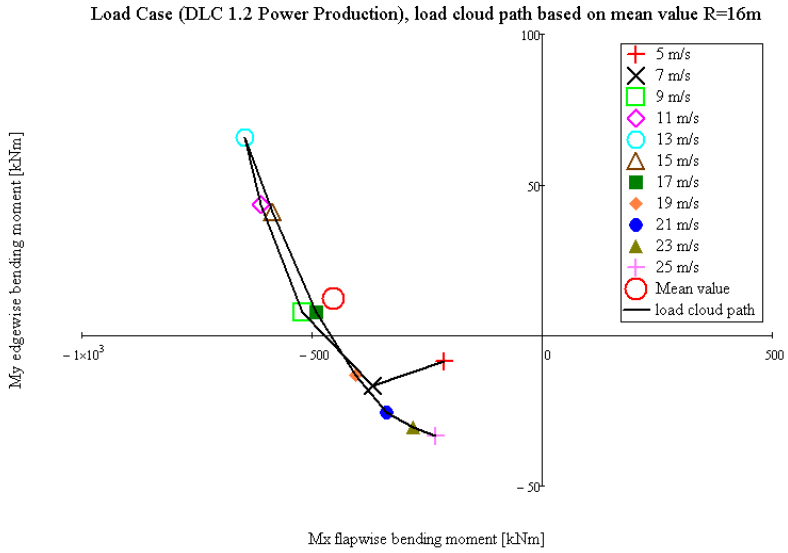

Figure 6: Load cloud path at cross section 16m

2.2.2 Normalized equivalent fatigue load based on the wind speed steps

The data available from aeroelastic simulations were applied to compute the normalized equivalent fatigue load at the different wind speed steps. This was performed by applying rainflow counting of the flap-wise and edge-wise loads separately. The method used for the rainflow counting is taken from Amzallag et. al. [3] and a user-specified 100 bins were applied. A slope of m=8 was assumed.

Via this method most of the damage from the flap-wise loads occurs from 17m/s to 25m/s while most of the damage generated by the edge-wise loads occurs from 9m/s to 15 m/s.

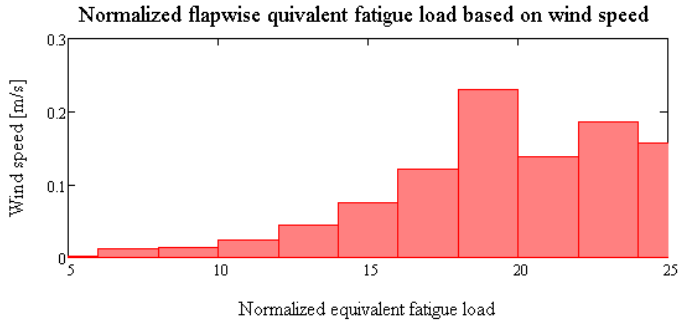

Figure 7: Normalized flapwise equivalent fatigue load computed based on the different wind speed steps

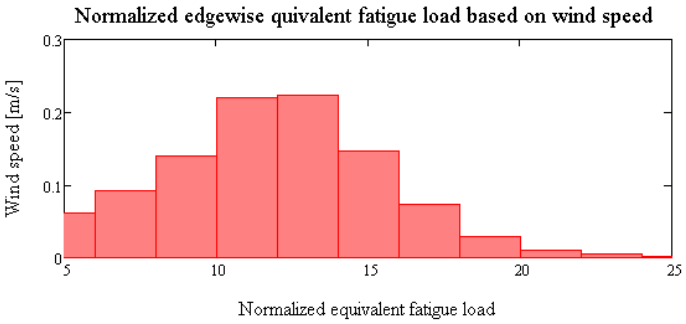

Figure 8: Normalized edgewise equivalent fatigue load computed based on the different wind speed steps

2.2.3 12 second samples of the load cloud at different wind speeds

In Figure 9 and Figure 10 small 12 second samples for 5m/s, 9m/s, 13m/s, 17m/s, 21m/s and 25m/s are plotted. From these plots it is clear that the loading paths which the turbine blades are subjected to in normal operation are very complex. The edge-wise loading is mainly dominated by gravity loads and the amplitude does not change significantly for different wind speeds. The flap-wise loading is on the other hand dominated by the wind speed and the pitching algorithm. By combining the flap-wise and edge-wise loads, which are what the blades are subjected to in reality, it becomes clear that the loading directions change significantly during these small samples.

2.3 A simplified example of a Dual-axis Resonance Fatigue Test

The most common fatigue test method today is the single-axis resonance approach which consists of two tests: A flap-wise and an edge-wise fatigue test where the blade is subjected to an equivalent loading which should mimic the entire operational lifetime over a short period (typically 1-2 months). In the standard IEC 61400-23 [4] it is stated: *The mean loads applied during fatigue testing shall normally be as close as possible to the mean load at the operating conditions that are most severe to the fatigue strength.* In common practice the mean loading in operation is often not applied. The only preload comes from the gravity load of the blade and the additional masses added to fine- tune the strain distribution along the blade span.

In Figure 11below is presented an example of a Dual-axis fatigue test including the mean loading for Design Load Case 1.2. The equivalent fatigue loads are increased so the test period is reduced to 1.2 months. In this simplified example the preloading and the masses which would be added is assumed not to affect the frequencies of the blade which would be the case in reality. In this setup the preloading is (Mx = -994 kNm and My =146kNm), the flap-wise frequencies is 1.09Hz and the edge-wise frequencies is 1.6Hz. The flap-wise equivalent fatigue load = 2245 kNm and the equivalent edge-wise fatigue load = 2161 kNm.

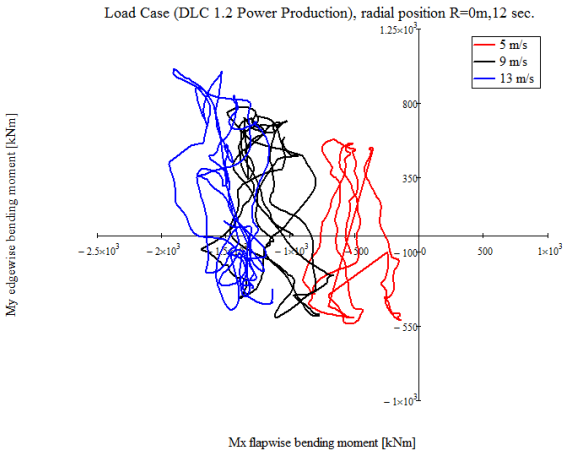

Figure 9: A 12 second sample of load cloud at 5m/s, 9m/s and 13m/s

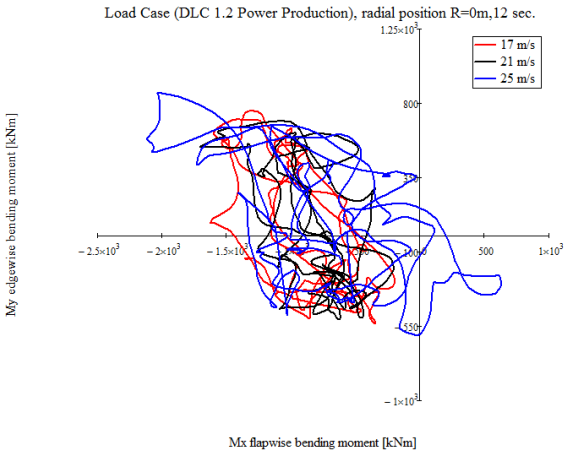

Figure 10: A 12 second sample of load cloud at 17m/s, 21m/s and 25m/s

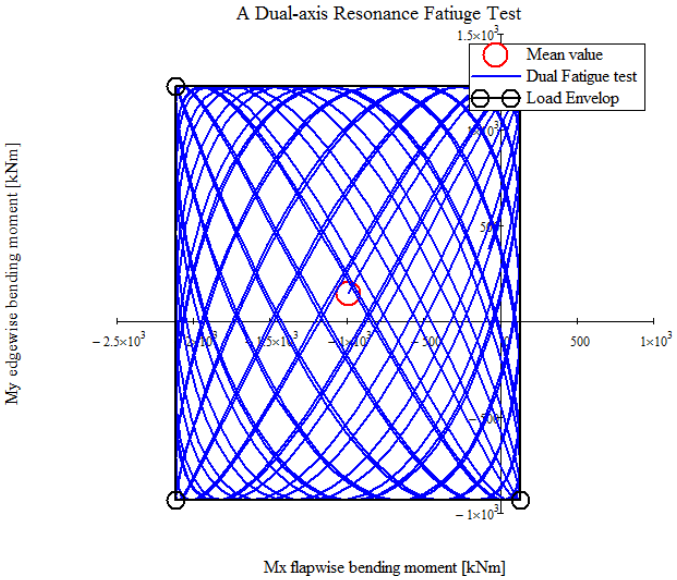

Figure 11: An example of a Dual-axis Resonance Fatigue Test

2.4 Analysis of principal fatigue load directions in blades of different scales

2.4.1 Evaluation of structure damage

The present IEC certification procedures [4] suggest that fatigue life of a wind turbine blade component is to be assessed by taking into account complex load states of the blade and stress values corresponding to these complex load situations. The fatigue damage is then to be evaluated based on the fluctuations of stresses within the blade structure.

Let us consider fatigue damage evaluation in more details. Initially, material tests performed on composite materials provide, among other information, so-called S-N curves. The S-N curves specify number of cycles (N) the particular material will survive under cyclic stress of given amplitude (S). The same curves can be expressed in terms of strain amplitude versus number of cycles. One of the most critical areas in a wind turbine blade is the blade root where highest bending moments occur. For the blade root cross-section, circular in shape, the highest axial stress σ_{max} within the cross-section with outer radius R_{outer} and second moment of inertia I is a simple linear function of the applied bending moment M:

$$\sigma_{max} = \frac{R_{outer}}{I} \cdot M \tag{1}$$

Therefore, fluctuations of the axial stress component which produce highest fatigue damage at the blade root can easily be calculated from the bending moments acting at the blade root. This simple linear moment-stress relation leads to a common fatigue damage assessment based on aeroelastic calculations of the entire wind turbine in certain design load cases (DLC) and further direct processing of the time series of the blade root bending moment.

When it comes to fatigue testing of wind turbine blades, this is most often done by splitting the bending moments into two principal components: Flap-wise and edge-wise bending moments. It is done for simplicity of the fatigue test rig and load application procedures. Rarely the two bending moment components are combined and applied simultaneously by exploiting certain methods and mechanisms. Due to difference in the natural frequencies of blade first flap-wise and edge-wise mode shapes the blade movement during the combined bending moment application test reminds Lissajous figures.

It is clear that the existing methods for assessing fatigue damage of wind turbines are first of all aimed at the blade root area which by coincidence (due to cross-section symmetry and high homogeneity in material distribution) leads to curtain simplicity in these methods. However, even for the simple maximum stress relation in eq. (1) one might notice that the part of the blade root that is damaged by the fluctuating bending moment is actually defined by the orientation of the bending moment itself. Damage accumulated in the blade root is not uniform. The damage distribution along the blade root highly depends on the fluctuation of the bending moment orientation i.e. on relation between the flap-wise and edge-wise moment components. The problem of non-uniform damage distribution through the cross-section becomes even more prominent in the non-symmetric blade cross-sections away from the blade root.

The described problem suggests a detailed study on load history analysis on blades where variation of both load directions and magnitudes in the blade structure are taken into account without separation of the bending loads into flap- and edge-wise components. An additional point of interest is to investigate if there is any size effect in the load distribution. This is to be done by considering blades of different scales.

2.4.2 Subject of study: Blades of three scales from MW-size wind turbines

Three wind turbine configurations are presently considered: NM-80 2.05 MW turbine with 34m SSP blades [2], NREL 5MW reference turbine and DTU 10 MW reference turbine. Difference in power rating and blade lengths for these turbines allows for observing scale effects in terms of variation of principal fatigue loads and their directions, if any. Hence, three blades of three different lengths and masses are taken into account hereby:

1. 34m (4.6 tonnes) SSP blade from the 2.05 MW NM-80 turbine
2. 62m (17.7 tonnes) blade from 5 MW NREL reference turbine
3. 86m (54 tonnes) blade from 10 MW DTU reference turbine

Each of the three wind turbines are simulated in aeroelastic code HAWC2 for a set of DLC (provided by the Aeroelastic Design section in DTU Wind Energy department). According to IEC [4] the DLC 1.2 (normal operation) is most important for the study on structural fatigue as blade sees this load case for ca. 95% of its lifetime. Therefore, only DLC1.2 is considered further. DLC 1.2 assumes simulation of wind turbine operating in a range of conditions during which fatigue damage is to be calculated. The conditions include:

1. A set of wind speeds following Reyleigh distribution
2. Three wind yaw cases for each wind speed: -10°, 0°, +10° with 25%/50%/25% time distribution accordingly
3. Each case above is to be modelled with 6 turbulence seeds 10 minutes long each.

Wind speed distribution for the NM-80 turbine is from 5 to 25 m/s with a 2 m/s step. For the 5MW and 10MW turbines wind speed ranges from 4 to 26 m/s with the same step, see Figure 12. Finally, effects of all the DLC1.2 load conditions are scaled with proper weighting factors.

.

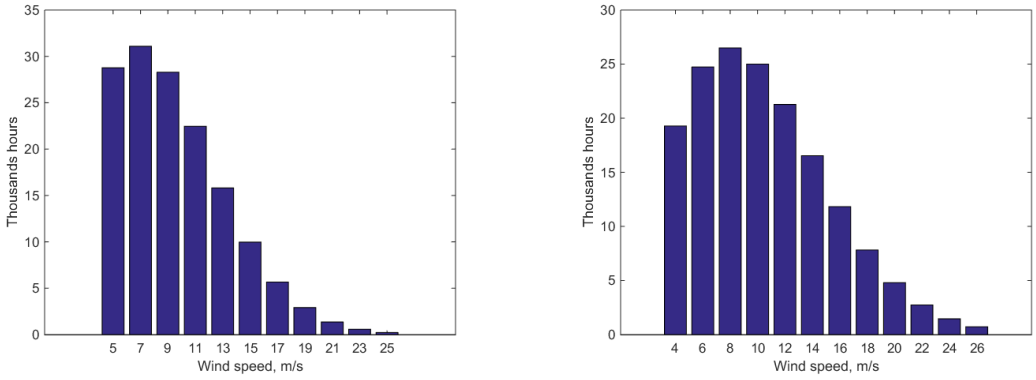

(a) (b)

Figure 12 Wind speed distributions for time simulations for 2.05 MW wind turbine, (a), and 5 and 10 MW wind turbines, (b).

2.4.3 Analysis of the blade fatigue load directions

Time series of the blade flap-wise and edge-wise root bending moment components are obtained as direct outputs from the HAWC2 simulations. Short example segments of these time series are given in Figure 13. Usually, from this point the two signals are processed separately and the fatigue damage associated with bending moments is split into damages from flap-wise bending moment and edge-wise bending moment.

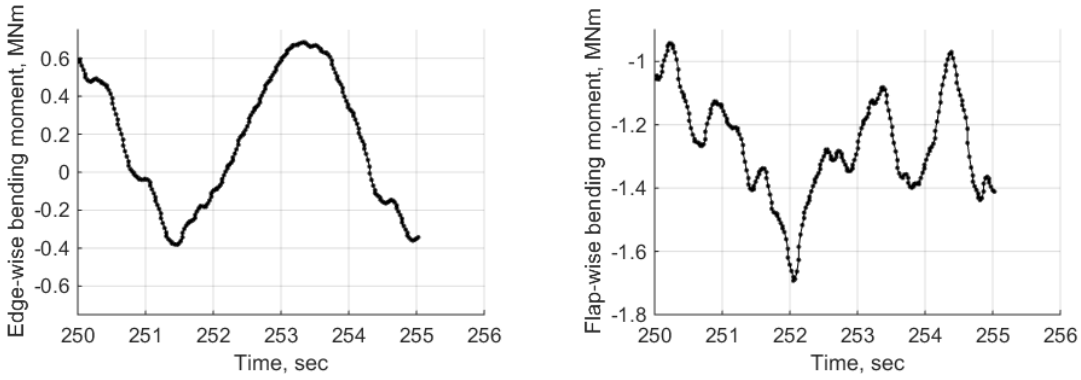

(a) (b)

Figure 13 Time series segments of edge-wise, (a), and flap-wise, (b), bending moments.

Presently, the separated time series are not of interest and instead attention is paid to the time series of the bending moment trace, see Figure 14. One of the main assumptions here is that the magnitude of the total bending moment does not directly contribute to the fatigue damage but the increments of the total bending moment do (bending moment offset, that is the magnitude of the average total bending moment can be considered at a later stage).

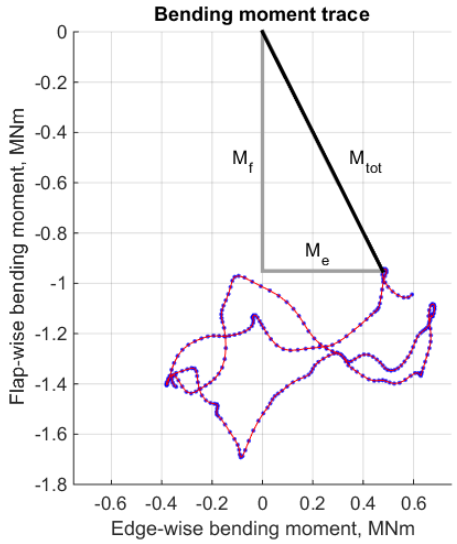

Figure 14 Segment of total bending moment M_{tot} trace for 2 MW wind turbine in 9 m/s wind conditions. Unprocessed trace, red line, is the same as the original trace, blue dotted line. M_f – flap-wise component, M_e – edge-wise component.

At initial stage, the bending moment traces from all DLC1.2 load condition simulations are taken as is and normalized direction diagrams of the bending moment increments for the blade root and blade mid-span cross-sections are calculated for each of the three blade configurations, see Figure 15. In all the cases apparent maximums in load increment directions can be noticed. For the smaller SSP blade the maximum is more inclined towards the edge-wise direction (ca. 170°), while for the two larger blade configurations the primary maximums are more inclined towards the flap-wise direction (ca. 120°) and the secondary maximums are quite symmetric to them (ca. 70°). The distribution patterns are similar for both blade root and mid-span cross-sections for all blade configurations.

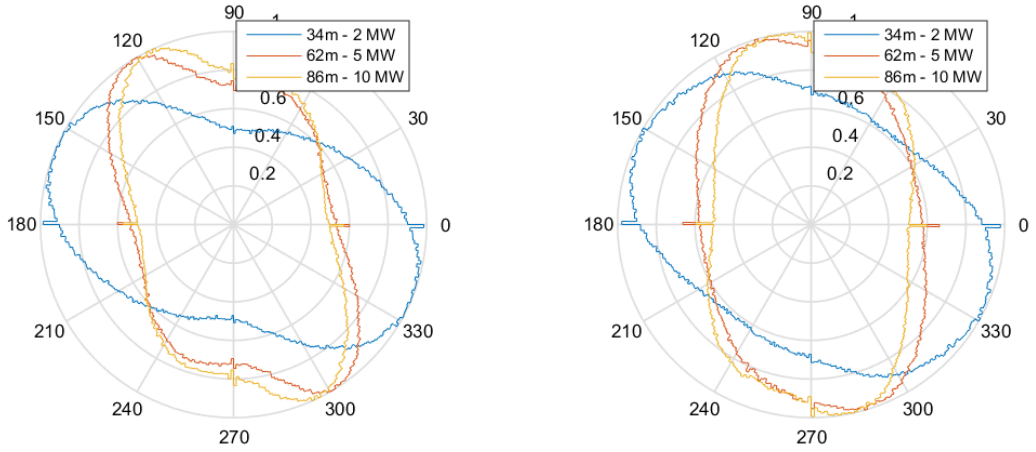

Figure 15 Distribution of the DLC1.2 original bending moment increments by direction. Normalized by maximum value.

At a glance, the obtained load increment distributions indicate that smaller blades possess higher edge-wise bending load fluctuations. This is an interesting observation; however, such a straight forward analysis of the load trace is not indicative as it is at least dependent on the simulation time step which directly affects the amplitude of the load increments. Therefore, the unprocessed raw load trace is filtered to exclude small load increments and to account only for highest load fluctuations within the simulation period. An example of the filtered results is shown in Figure 16 and the filtered loading diagrams for all DLC1.2 simulations are presented in Figure 17. For all the blade configurations the load direction maximums became more prominent. For the blade roots the 34m blade load maximum did not significantly change its direction while the maximums of larger 62 and 86m blade became more edge-wise oriented. In contrast, for the blade mid-span positions the maximums did not turn for all blade configurations.

The bending moment increment direction diagram in Figure 17 is obtained as weighted sum of all the increment amplitudes in each direction and does not really have any physical meaning, rather than pointing out that there are some dominant load increment directions and actually showing these directions. Logically, the next step would be to look at the fatigue damage done by these load increments and to see if the damage direction diagram has any distinctive peaks. So far there is no recognized method for performing such analysis and rather simplified approach is presently used.

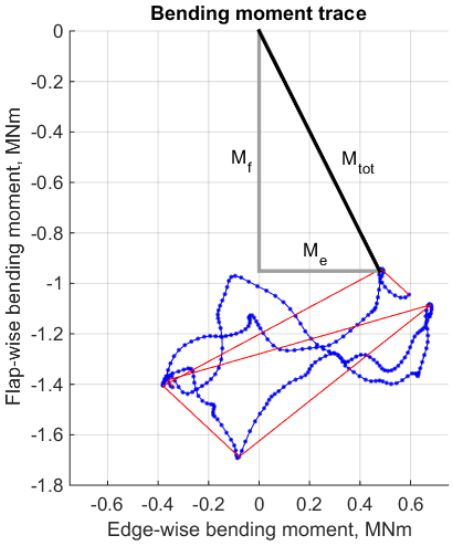

Figure 16 Segment of total bending moment M_{tot} trace for 2 MW wind turbine in 9 m/s wind conditions. Unprocessed original trace, red line, and filtered trace, blue dotted line. M_f – flap-wise component, M_e – edge-wise component.

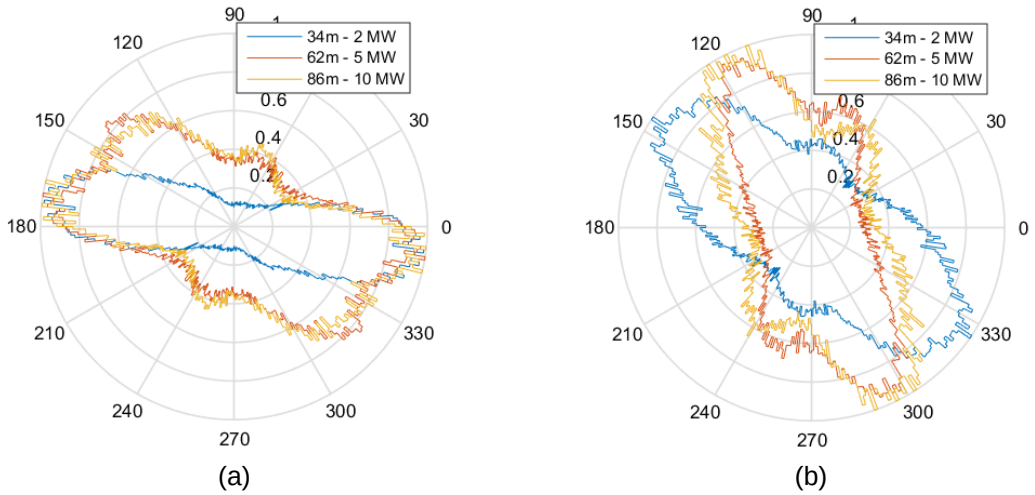

Figure 17 Distribution of the DLC1.2 filtered bending moment increments by direction. Normalized by maximum value.

As stated in the beginning, maximal stress magnitude and its position within a generic cross-section are highly dependent on the bending moment magnitude and orientation. To overcome this complication it is presently assumed that the stress magnitude does not depend on the bending moment orientation (like in symmetric blade root cross-section) but only the position of the highest stress in cross-section is a function of load orientation. This assumption leads to simple linear stress-bending moment relation as in eq. (1) and the possibility to use Miner rule [5] to assess fatigue damage due to each load increment in each direction. Presently, the S-N slope parameter m for the glass-fiber reinforced plastics material all three blades are composed of is taken as 8. The calculated fatigue damage distributions for blade root and blade mid-span cross-sections are presented in Figure 18.

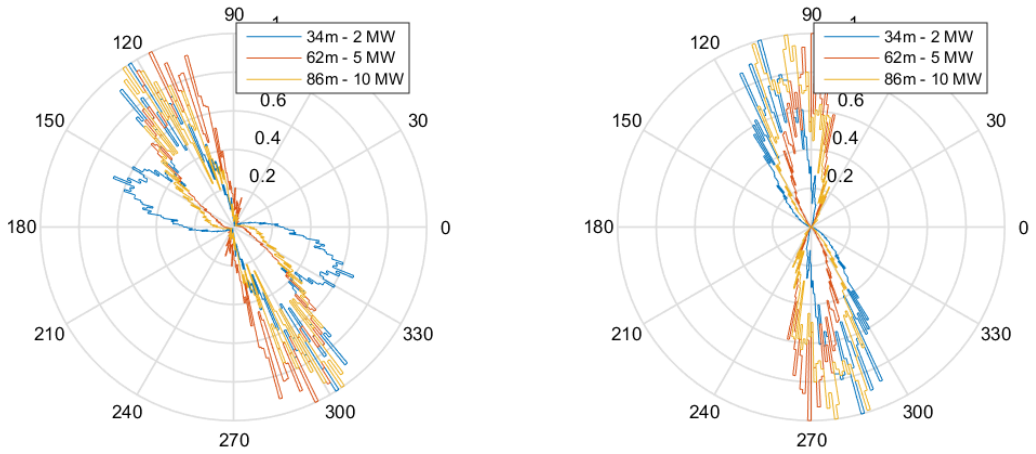

Figure 18 Distribution of the DLC1.2 damage (m=8) from bending moment increments by direction. Normalized by maximum value.

One can observe that there are distinctive maximums in damage direction diagrams for all three blade configurations and at both blade root and mid-span cross-sections. For the root cross-sections it is interesting to note that most of the damage is accumulated at ca. 120° direction which is predominantly the flap-wise direction. This is different from the results in Figure 17 indicating that even though most of the load increments are aligned with the edge-wise direction, higher damage is still done in another direction with fewer cycles but with higher amplitudes. In fact, the S-N curve slope parameter m is the well-known factor stipulating this damage amplification effect. For the shorter 24m blade there is a secondary local damage maximum in the 150°-160° direction which indicates that there might still be significant damage accumulated in the near edge-wise direction.

For the blade mid-span cross-sections, Figure 18b, the results show that the fatigue damage is predominantly accumulated in flap-wise direction. Recalling the main assumption of the given damage analysis procedure, one should be careful treating this result, as in the blade mid-span position the cross-section is an aerofoil, very far from a axisymmetric shape and the validity of the assumption is lower there.

2.5 Conclusions and recommendations

The presented analysis of the fatigue loads in the blades of different scales demonstrated that the load fluctuations contributing to blade fatigue damage are unevenly distributed direction-wise and predominant fluctuation directions are visible.

It was observed that for the smaller scale blades the load increment are oriented more towards the edge-wise direction while for the larger blades are oriented more flap-wise. Remarkably, if the accumulated fatigue damage is calculated according to the method presently proposed the major damage is found to be in the direction of ca. 120° which is close to the flap-wise direction. The observed size effect indicates that roots of the blades of smaller scales accumulate significant amount of damage in the near edge-wise direction while larger blades show damage predominantly closer to the flap-wise direction.

The assumptions and methods adopted in the present study did not prove to be reasonably consistent in order to be recommended for further use and are subject for subsequent improvements. Nevertheless, the obtained results demonstrate that distinct predominant fatigue loading directions in wind turbine blades might exist and they are not solely flap-wise or edge-wise. With further development of the directional fatigue analysis method the results can be used for better predicting fatigue life of blade components and for formulating more specific requirements for fatigue testing of blades of different scales.

3. Advanced measuring methods for blade testing

3.1 Introduction

The experimental results presented in this report were part of an experimental blade research program that was conducted in the blade testing facility at DTU Risø campus. The research project was concerned with investigations of the deformation behavior at low load levels as well as with the local stability failure at ultimate limit state of a 34m full scale wind turbine blade. Figure 19 shows a schematic representation of the test setup. The blade was mounted at an eight degree angle with respect to the horizontal direction in order to increase the available space for deflection. The blade was mounted in a way that the suction side is facing the ground. The blade was pitched by -30 degrees which represent a combined edgewise-flapwise loading case. All the blades tested are of the same type and have been reinforced in the web joints in order to prevent local shear buckling. As shown in Figure 19 and Figure 20, the blade was loaded at four loading points. The procedure and specifications of loading will be discussed in the following sections. It should be mentioned that in the current report the main focus is to compare the results from three different tests namely blade #3, blade #4 and blade #5. Comparisons are made in terms of global stiffness of the blades and in terms of evaluation of the data quality.

This section explains the adopted sensors and measurement techniques used for blade #5.

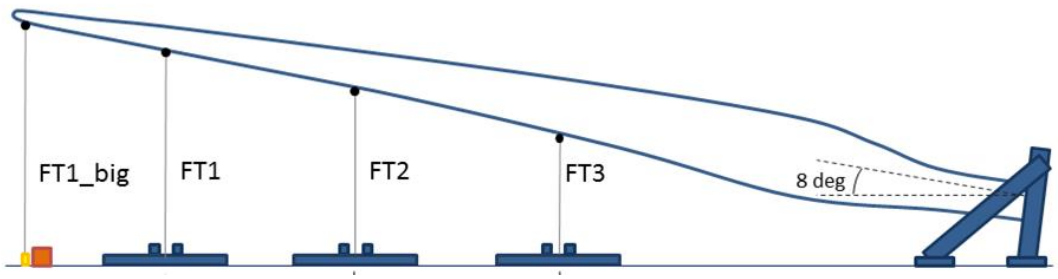

Figure 19 Test setup of 34m wind turbine rotor blade loaded at four points and pulled towards the floor by winches via a pulley system.

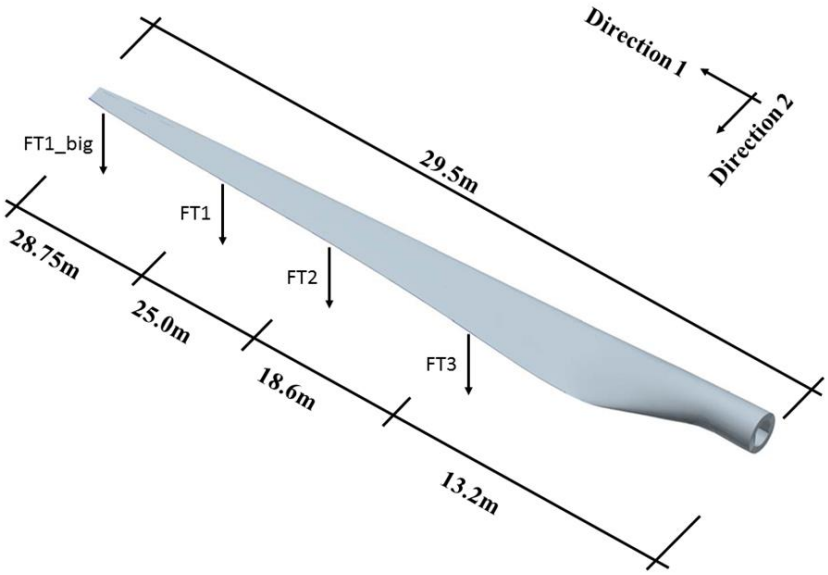

Figure 20 Blade directions and dimensions. The sensors are referred to longitudinal and transversal as shown in this Figure.

3.2 Data Acquisition System: DAQ

3.2.1 Sensors and Force Transducers

In Blade Test #5 forces were individually measured by force transducers in every loading point. In addition, six draw wire transducers (ASMs) sensors were used to measure the vertical displacements in the caps and at designated points along the trailing edge. Electrical resistance strain gauges and Fiber Bragg Grating strain gauges were used to measure longitudinal and transverse strains in vicinity to the trailing edge between 10m and 23m. Table 3 summarizes the sensors used in blade test #5. All the mentioned sensors in Table 3 except the Fiber Bragg Grating sensors are connected to 4 *Hottinger Baldwin Messtechnik* (HBM) collectors named as CanHeads and then subsequently connected to the HBM main amplifier system MGCPlus. The amplifier is connected to a PC and the data is accessible through a GUI called CatmanEasy. Figure 21 shows the channels list in the data acquisition (DAQ) system. The data sampling rate was 1Hz.

In addition, four Computational Channels were prepared for calculating the loading error according to the target loads. Different output files could be extracted from every sampling session. It was chosen to select the ASCII file type which includes the channel names. Figure 22 shows the designed DAQ system panel while working. In this panel the loads, displacements and errors of loading were put on display in order to facilitate and control the loading. To illustrate the errors in the panel two methods were used. Computational channels in the CatmanEasy software were used to present the error in real time and EasyScript feature of the GUI software was used to measure the error every time the prepared script is called. The second method offered a wider range of operations and segments that could be used in the code. On the other hand the script in the real time channels was limited to a few lines only.

Table 3 Sensors table for blade 5.

Sensor	Measurand Unit	QTY	MFR	Model	Specifications
Force transducer	kN	4	HBM	S9 and K12	50kN = 2mV/V Tension
Displacement sensors	m	4	ASM	PosiWire 6250, 4000, 2000	4 on cap on suction side at 29, 22, 16, 10 m from the root
Displacement sensors	m	2	ASM	PosiWire 2000	2 on trailing edge at 13 and 16 meters from the root
Electrical resistance strain gauges	$\mu m/m$	8	HBM	micro SG 2.06	4 On the root and 4 around 10m from the root
4 switch sensors for winches	-	4	-	-	One for each winch
Fiber Bragg Grating strain sensors	$\mu m/m$	160	Fiber Sensing		40 longitudinal with 40cm distance on pressure side, 40 longitudinal with 15cm distance on pressure side, 40 transversal with 15cm distance on pressure side, 40 transversal with 15cm distance on suction side

The Fiber Bragg Grating sensors are connected to the amplifiers called BraggMeters and produced by the sensors manufacturer (FiberSensingHBM). Each amplifier case can be connected to 8 channels. Every channel can accommodate a different number of sensors, up to 25 sensors in total. The amount of sensors is a function of the available strain range. The theory and implementation of these sensors are explained in the next section. In the current project 10 sensors were used in every channel. With 2 BraggMeters 160 sensors have been used in total. The BraggMETERs were connected to a PC through a developed interface by the manufacturer. The data sampling rate of this system is 1Hz. The interface is called BraggMonitor. The specification of the system is explained in the next section.

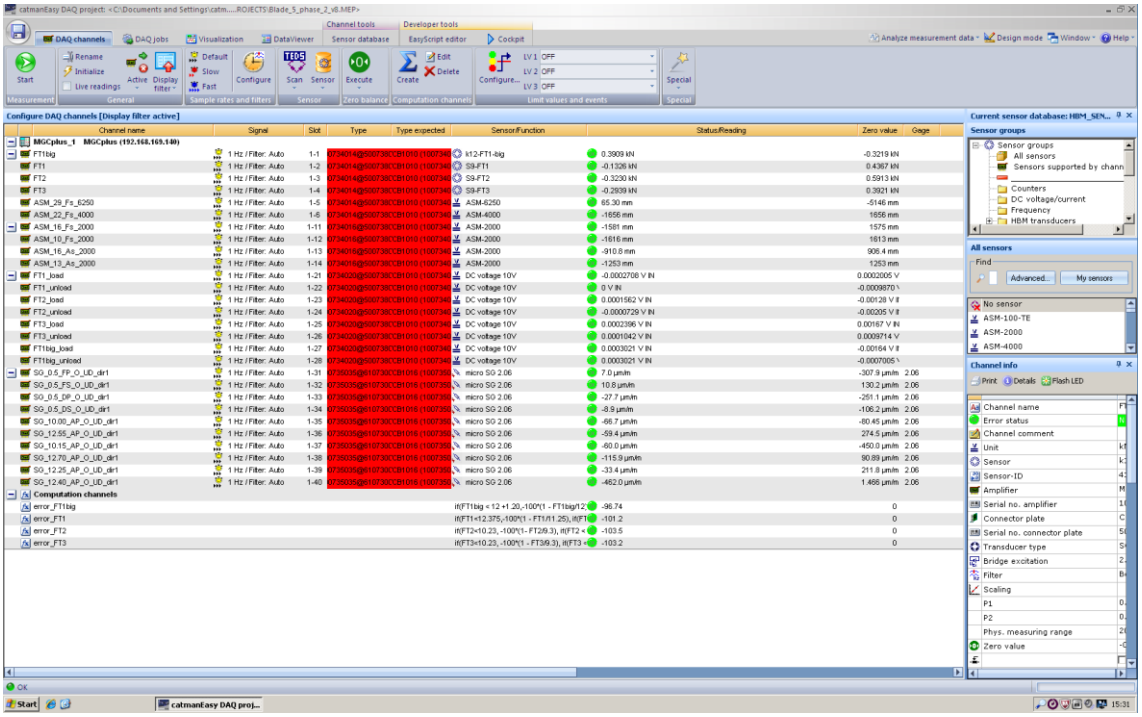

Figure 21. Channels and sensors used in the test shown on the user interface.

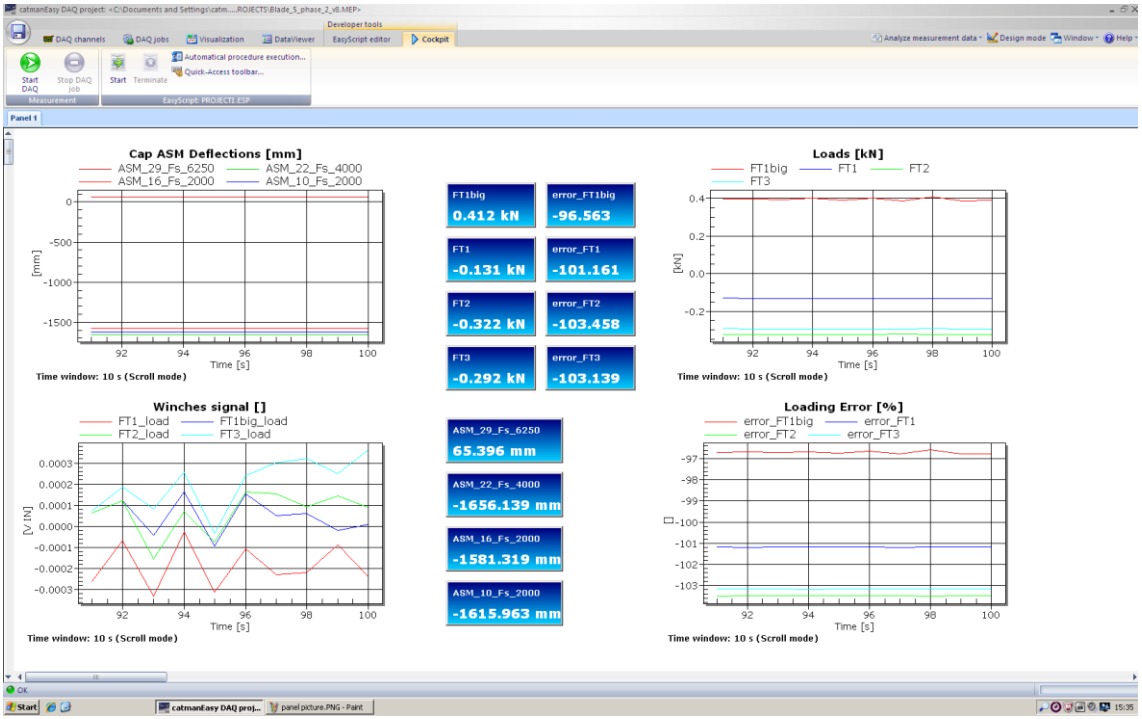

Figure 22. DAQ panel as displayed during testing showing individual loads, load errors and the ASM readings in real time.

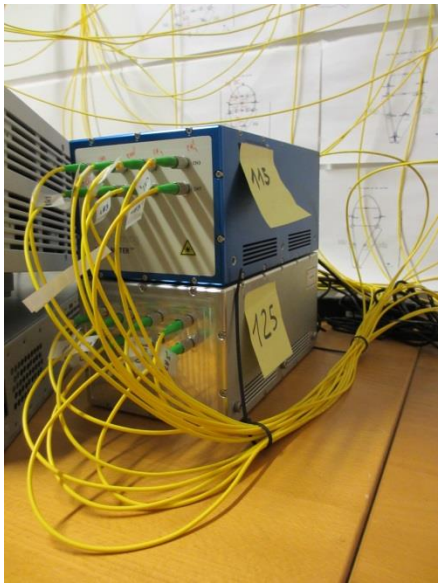

Figure 23. Two BraggMeters with 8 channels used in the ultimate test.

3.2.2 Fiber Bragg Grating

The basic concept of Fiber Bragg Grating is based on the principle that an optic fiber with a patterned defect at a certain point will reflect the optic wave at a certain wave length. As shown in Figure 24, if a light wave is sent through the fiber, all the waves will pass except waves around a certain frequency which cause a peak in the reflected wave spectrum. By exposing this defected part (i.e. sensor) to strain the peak of the spectrum of reflected signal will shift to higher or lower frequencies. The reflected signal can as well be investigated in the wavelength domain instead of the frequency domain. The wavelength is calculated by dividing the speed of light in the fiber over frequency. The change in the wavelength is directly proportional to the magnitude of tension or pressure strains according to equation 2.

$$\frac{\Delta\lambda_B}{\lambda_B} = C_S\varepsilon + C_T\Delta T \tag{2}$$

where C_S is the coefficient of strain and C_T is the coefficient of temperature. In the current test since the temperature does not change during the test period the second term on the right hand side is neglected.

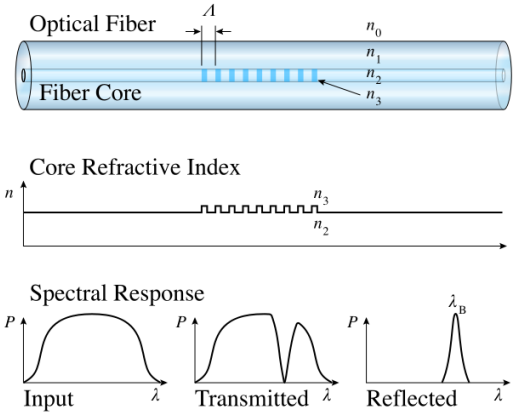

Figure 24. Fiber bragg sensing principle showing reflected wave as a peak in the power output diagram.

The operating range of the BraggMETER is between 1500 to 1600 nm. The Maximum recommended number of sensors in every channel is 25 with a range of ±2 nm. But since the strain magnitudes exceed this limit in test #5, the number of sensors in every channel was limited to 10 in order to increase the band width to ±5 nm. (a small distance between the range of each two sensors should be considered.) Neglecting the effect of change in the denominator of equation 2 the relation of the strain and change in wavelength can be reduced to:

$$\varepsilon\ [\mu m/m] = 1000\ (\Delta\lambda\_B)/1.2 \tag{3}$$

Specifications of the used system is shown in Table 4:

Table 4 BraggMETER specification table.

Range of wavelength measurement	100 nm (1500 to 1600nm)
Resolution	1.0 pm
Control interface	Ethernet (TCP/ IP)

The output file of the BraggMETER system is a tab separated text file. Figure 25 illustrates the layout of the Fiber Bragg Grating sensors as applied on the blade. The sensors were installed in order to measure strains along both the longitudinal and the transversal blade directions. In the former direction two different fiber lines were used and placed on the pressure side of the blade about 13cm away from the edge. The first one reached from 10 m to 24 m with 40 cm spacing between sensors, while the second one, with a 15 cm resolution, measured strain only in the region between 10 and 16 m from the root. This configuration was chosen since blades 3 and 4, previously tested to failure, broke in this particular region. Similarly, transversal strains (perpendicular to the blade axis) were measured with the same 15 cm resolution on both the suction and pressure side of the blade. In the failure designated area, between 10 and 16 m from the root, the longitudinal and the transversal sensors were installed as close as possible without creating interference issues to the fibers, in order to have two-direction strain measurement points on the blade trailing edge.

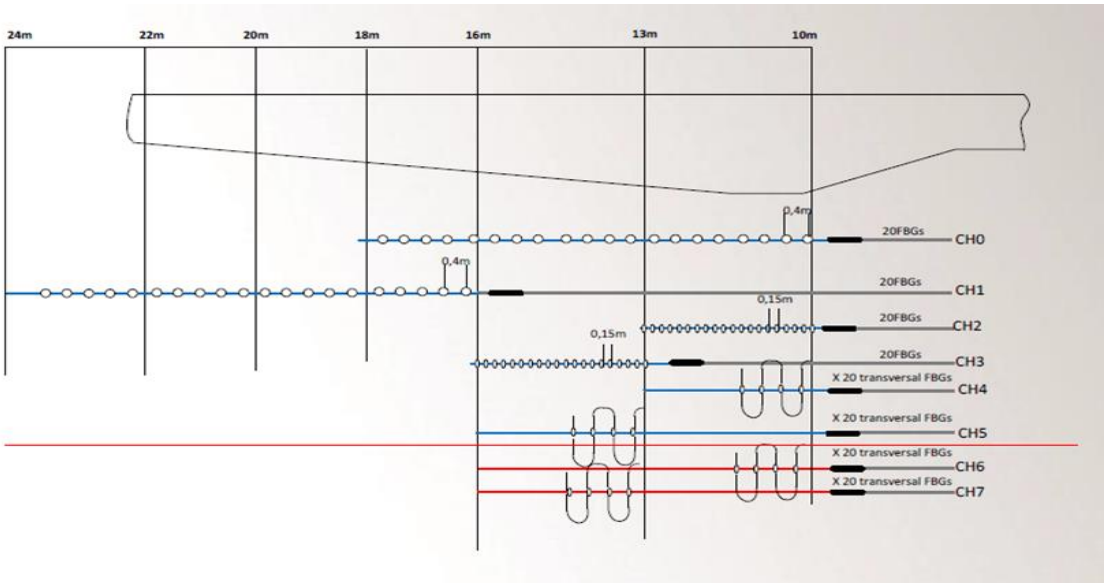

Figure 25. Sensor layout along trailing edge with fine resolution array every 15cm and coarse resolution array every 40cm spacing. Transverse strains measured every 15cm.

3.2.3 Synchronization

A MATLAB function was used to synchronise the three output files from three DAQ systems. As already mentioned one of the output files is ASCII file while the other two in tab separated text files related to the FBG system outputs. The function takes the address of the files as an input and then based on the starting time of the files separates the one part of each file that is common between all the output files. The output is a structure file including all the data with only one time vector.

3.2.4 Data Analysis MATLAB script

Two separate Data Analysis scripts were developed based on the existing codes from previous projects. These scripts are made in a way that after providing the test folder the synchronisation function will find the output files and return a structure that contains the required data. The next step involved the recognition of the loading steps since the steps have been changed throughout several pre-tests. This is done with another function which recognises the steps based on the behaviour of the force transducers. These scripts enabled the data analysis for each test a few minutes after the test with little modifications of addresses and tuning the standard deviation of the loading steps to get the correct number of steps.

3.3 Stereo photogrammetry

3.3.1 Theory

An in-house stereo photogrammetry based measurement system was adopted to measure the local buckling deformation in the designated failure area. These measurements serve the purpose to validate the measurements obtained from the fiber sensors and to identify the onset of the buckling wave. Prior to ultimate failure, a buckling wave appears. It is therefore, of interest to study the area on the blade where the buckling wave is expected to occur. For this

specific blade, a buckling wave was expected to appear in the area between 13m and 16m measured from the root.

The idea behind the stereo-photogrammetry method is to have two images of the same physical object from two cameras with different angles to the object. The method has two steps, namely a calibration step and a triangulation step. In the calibration step, the known real-world coordinates of a calibration object are linked to the corresponding pixel coordinates of the calibration object in the two images. In the triangulation step, the pixel coordinates of the target object in the two images can be used to determine the real world coordinates of the object. In this way, a moving physical object can be tracked by the two cameras. The calibration and triangulation steps used here are based on Shmueli *et al.* [6].

In the calibration step, the calibration parameters are assembled in a calibration vector C defined as:

$$C = (D^T D)^{-1} f \tag{4}$$

where the column vector f contains the pixel coordinates of the calibration points (u_n; v_n), where n is the number of calibration points. The vector f is thus given as

$$f = [u_1, v_1, u_2, v_2, \dots u_n, v_n]^T \tag{5}$$

The matrix D is given as

$$D = \begin{pmatrix} x_1 & y_1 & z_1 & 1 & 0 & 0 & 0 & 0 & -u_1x_1 & -u_1y_1 & -u_1z_1 \\ 0 & 0 & 0 & 0 & x_1 & y_1 & z_1 & 1 & -v_1x_1 & -v_1y_1 & -v_1z_1 \\ x_2 & y_2 & z_2 & 1 & 0 & 0 & 0 & 0 & -u_2x_2 & -u_2y_2 & -u_2z_2 \\ 0 & 0 & 0 & 0 & x_2 & y_2 & z_2 & 1 & -v_2x_2 & -v_2y_2 & -v_2z_2 \\ \vdots & \vdots & \vdots & \vdots & \vdots & \vdots & \vdots & \vdots & \vdots & \vdots & \vdots \\ x_n & y_n & z_n & 1 & 0 & 0 & 0 & 0 & -u_nx_n & -u_ny_n & -u_nz_n \\ 0 & 0 & 0 & 0 & x_n & y_n & z_n & 1 & -v_nx_n & -v_ny_n & -v_nz_n \end{pmatrix} \tag{6}$$

where x_n; y_n; z_n are the real-world coordinates of the calibration points. The calibration vector C can thus be determined from equation 4.
The triangulation step determines the real-world coordinates of the target object from the pixel coordinates in the two images. The entries in the calibration vector C are now denoted as follows

$$C = [c_{u1}, c_{u2}, c_{u3}, c_{u4}, c_{v1}, c_{v2}, c_{v3}, c_{v4}, c_X, c_Y, c_Z]^T \tag{7}$$

A C-matrix is computed for each of the two images. Solving the matrix system of linear equations

$$[X, Y, Z] = [P][t]^{-1} \tag{8}$$

gives the real-world coordinates [X; Y;Z] of the target object. The matrix P is given as

$$P = \begin{pmatrix} c^1_{u1} - u_1 c^1_X & c^1_{u2} - u_1 c^1_Y & c^1_{u3} - u_1 c^1_Z \\ c^1_{v1} - v_1 c^1_X & c^1_{v2} - v_1 c^1_Y & c^1_{v3} - v_1 c^1_Z \\ c^2_{u1} - u_2 c^2_X & c^2_{u2} - u_2 c^2_Y & c^2_{u3} - u_2 c^2_Z \\ c^2_{v1} - v_2 c^2_X & c^2_{v2} - v_2 c^2_Y & c^2_{v3} - v_2 c^2_Z \end{pmatrix} \tag{9}$$

where the superscript 1 refers to the entries in the C-matrix for image 1, and the superscript refers to the entries in the C-matrix for image 2. The column vector t is given as

$$t = \begin{pmatrix} u_1 - c^1_{u4} \\ v_1 - c^1_{v4} \\ u_2 - c^2_{u4} \\ v_2 - c^2_{v4} \end{pmatrix} \tag{10}$$

3.3.2 Corner extraction

In order to accurately define a point on the target object, it is efficient to attach a black-white marker on the measurement object. The design of the marker should be such that there is a clearly defined black-white corner, as shown in Figure 26. Harris and Stephen [7] suggest a method to determine the corner point by examining the color gradient in the horizontal and vertical direction. The method used in the present work is also described in detail in [6]. The corner extraction method computes the color gradient in x- and y-direction within a search window and gives a best estimate for the pixel coordinates of the corner.

The calibration can be tested by using the extracted pixel coordinates of the corners as an input to the triangulation and thereby obtaining a set of predicted real world coordinates of the corners. The error on each corner in the calibration board is taken as the difference between the well-known real world coordinates and the predicted real world coordinates. In order to have a good calibration, this error should be minimized.

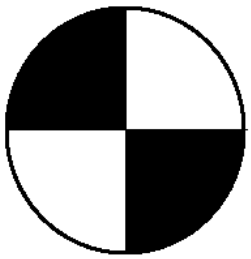

Figure 26. Black white crash test marker as used for the stereo photogrammetry based system.

3.3.3 Extracting the local displacement

The deformation of the blade can be expressed as the sum of the rigid-body deformation (St. Venant solution) and the local displacement (warping). The propagation of a crack in the blade

is associated with the local displacement, and therefore it is of interest to extract the local displacement. For this purpose the rigid body deformation is subtracted from the global displacement. This can be done by curve fitting techniques assuming higher order polynomial functions or taking deformations from linear finite element models.

3.3.4 Experimental setup

Two Casio EX-ZR200 digital cameras are mounted close to the wall at an elevated position facing the trailing edge of the blade, see Figure 27. The cameras are positioned such that they capture images of the trailing edge in the area between 12.5m and 15.95m from the root of the blade.

The calibration grid consists of a checker-board pattern mounted on a flat boards staggered in two different parallel levels. The upper part of the plate measures 1.30 x 0.45 m and the lower part measures 1.30 x 0.30 m. The difference in level is 50.6mm and the size of the squares in the pattern is 50 x 50 mm. The calibration grid is placed under the trailing edge of the blade. The focus planes of the cameras were aimed at the calibration grid.

To track the motion of the blade, the position of the trailing edge relative to the calibration grid is determined. This is done by extracting the position of the circular trackers mounted on the trailing edge from the images. The design of the markers used is shown in Figure 26.

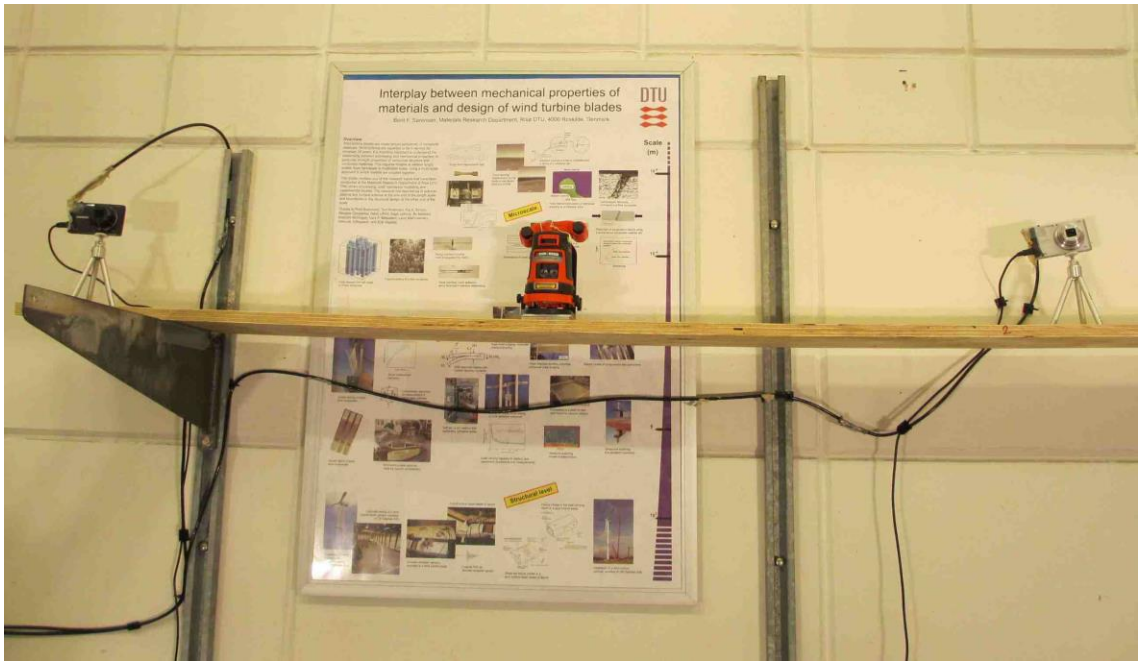

Figure 27. Measurement setup showing two digital cameras placed on a shelf next to the trailing edge running parallel to the wall shown in this image. A laser level (centre of image) was used to align the calibration grid. The digital cameras were electronically synchronised in such a way that images could be taken at the same instant of time.

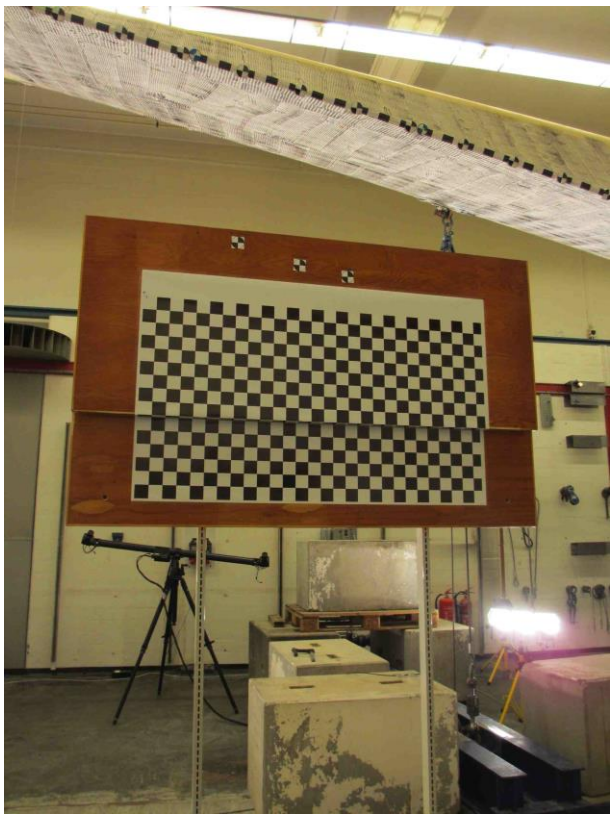

Figure 28. Calibration grid with two staggered planes 50mm apart with a grid size of 50mm mounted on two wooden boards placed in close vicinity of the measurement area. Three dummy markers with known coordinates in the upper edge of the grid used for accuracy checks.

The real-world coordinates of the markers (see Figure 29) are found by a calibration and triangulation as described in the theory section. A MatLab code based on the code written by Shmueli *et al.* [6] was implemented. The data processing procedure calibrates and tracks the markers and gives the real world coordinates of the markers as an output. The MatLab code requires the input of a first guess of the pixel coordinates of the 4 corners in both the upper and lower part of the calibration board. The first guess of the pixel coordinates of the calibration corners and the markers are typed in manually. The real world coordinate system is centered on the calibration board. A detailed description on how to use the software is provided in the report Small Displacement Measurement System - Documentation.

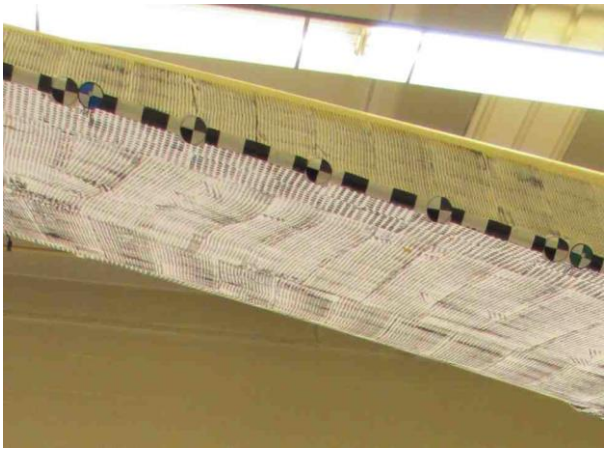

Figure 29. Markers placed along the trailing edge of the wind turbine blade with a spacing of 25cm.

A displacement sensor, ASM, was mounted at 12.95m and 15.95m and an additional marker was placed in each position. The displacement obtained from the sensors compared to the displacement results. Additionally, a simulation of the deformation was performed in Abaqus and can be compared to the SDMS results.

3.4 Loading

The target loads of the individual loading points that correspond to 100% Risø load are given in Table 5. Loads were applied at a constant ratio between individual load points.

Table 5 Loading description at the four loading points along the blade.

Channel name in DAQ	FT1big	FT1	FT2	FT3
Radial position from the root [m]	28.5	24.6	18.6	13
Maximum load [kN]	80	75	62	62

To apply the loads three electrical winches and a hydraulic winch were used. All the winches are connected to inverters. The speed of the winches was adjusted in order to apply loads more accurately. The electrical winch speed was reduced from 30 Hz to 20 Hz without affecting the winch torque but increasing the accuracy. Figure 30 shows the general layout of the loading system including the winch and the load cell (force transducer). It is noteworthy to say that with this configuration the load cell measured only half of the load applied.

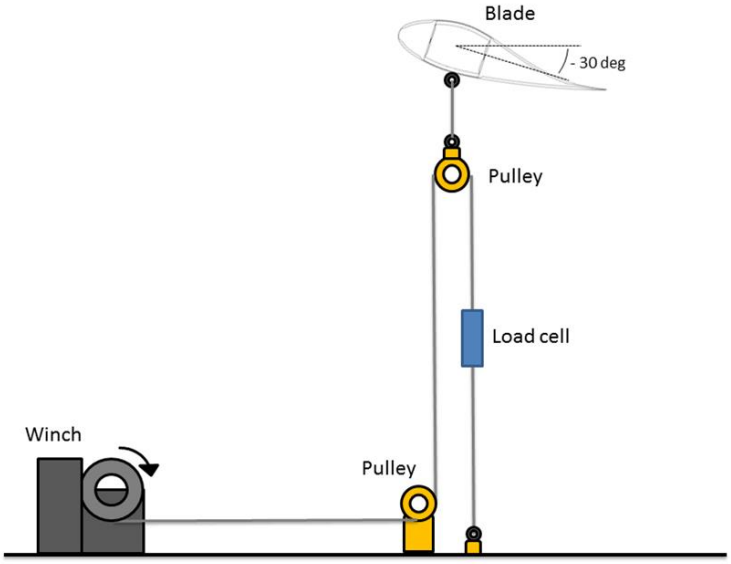

Figure 30. Schematic setup of the winch pulley arrangement showing a typical load application point with a load cell and the blade cross section with -30 deg. pitch angle.

3.4.1 Pre-tests

Before performing the final test several pretests were performed. Pretests from 1 to 12 (On 18/Sep/2014) were done with one loading point at the tip, whereas for pretests 13 to 22 (On 1/Oct/2014) four loading application points were used. The final test was performed on 2/Oct/2014.

The first set of pretests served the following purposes:

1. Calibration of the force transducers and sensors.
2. Comparison of blade stiffness.
3. Determination of size and position of the calibration grid.
4. Loading procedure investigation and loading error evaluation.
5. Validation of FBG sensors with electrical resistance strain gauges.

Tip loads were applied in 5 steps: 10, 20, 25, 30, 35 and 40 kN. Figure 31 shows the time history of loading in pre-test 12 where all load cells were connected in series for calibration purposes.

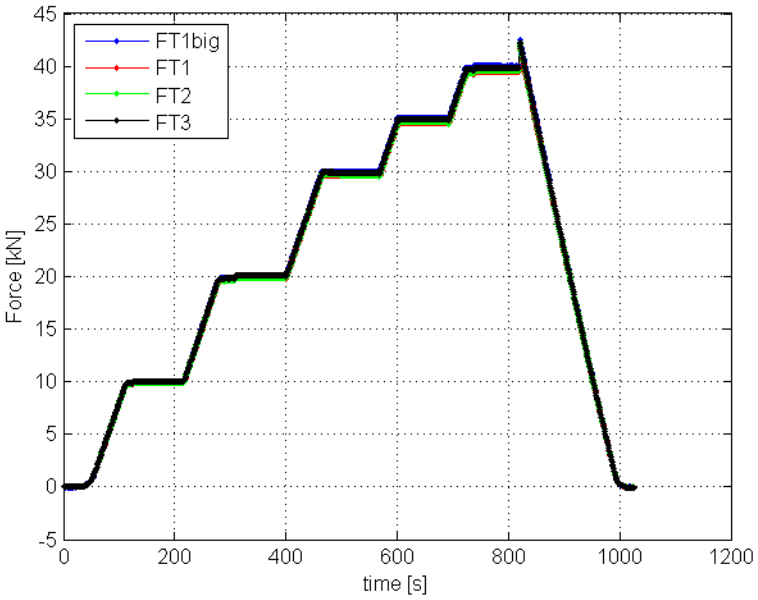

Figure 31. Time history of the loads applied in steps of 10%, 20%, 30%, 35%, 40%.

3.4.2 Four load application point tests

The four point loading scheme is a complex non-linear problem due to unloading phenomena owning to structural coupling effects. Whereas previously tested blades were loaded by applying forces simultaneously, a new loading scheme was adopted for blade 5.

In this scheme the winches were operated individually by increasing the displacement in one loading point until the individual target load was reached. This procedure was repeated in an iterative procedure until all target loads satisfied a deviation limit of 2%.

The load steps in the second set of pre-tests were set to 10%, 15%, 20%, 25%, 30%, 35% and 40% of the maximum loads on each loading point. The calculated error is based on Guide to Uncertainty Measurement prepared by ISO [8]. The uncertainty in the load distribution is assumed to be independent from each other and each component has the same effect on the total uncertainty. With these assumptions equation 11 will be reduced to equation 12.

$$u_c(y) = \sqrt{\sum_{i=1}^{N} \left(\frac{\partial f}{\partial L_i}\right)^2 u^2 L_i} \tag{11}$$

$$u_c(y) = \sqrt{\sum_{i=1}^{4} u^2 L_i} \tag{12}$$

where $u_c(y)$ is the uncertainty of loads (bending moment) distribution, u(L) is the uncertainty of each load and f is the function that relates these two variables together.

In Figure 32 the time history of loads for pre-test 18 is shown. Figure 33 and Figure 34 show the loading uncertainty for each step in pre-test 18.

The new loading procedure is more time demanding when compared with the old scheme as it requires a higher number of iterations required to reach convergence.

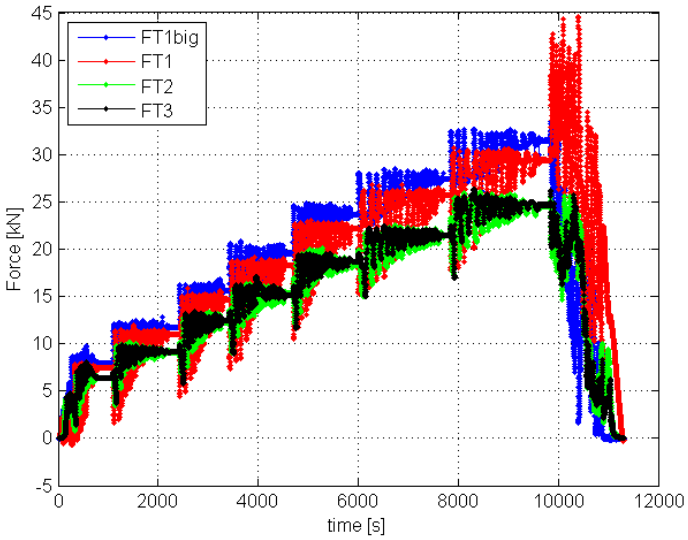

Figure 32. Time history for pre-test 18.

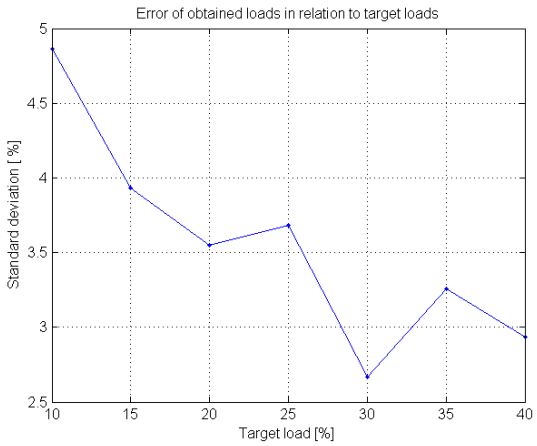

Figure 33. Loading error for each step of test-18.

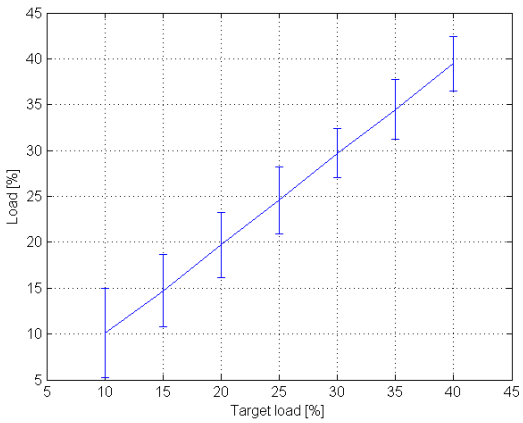

Figure 34. Loadings with error bars for each step for pre-test 18.

3.4.3 Ultimate Test

The same loading procedure was used for the ultimate test. Figure 35 shows the time series of the load points up to failure. In the ultimate tests the first load steps up to 30% were performed with a low number of iterations in order to decrease the duration of the test. This does not affect the validity of the data since load levels up to 30% were already covered by the pre-tests.

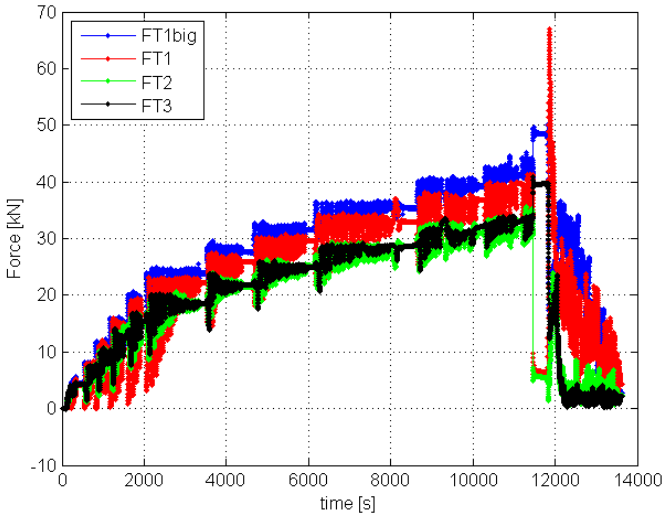

Figure 35. Time series of loading for blade 5 final test with four load application points.

Figure 36 shows the errors as a function of the load wheres Figure 37 shows the uncertainty band as a function of the target loads.

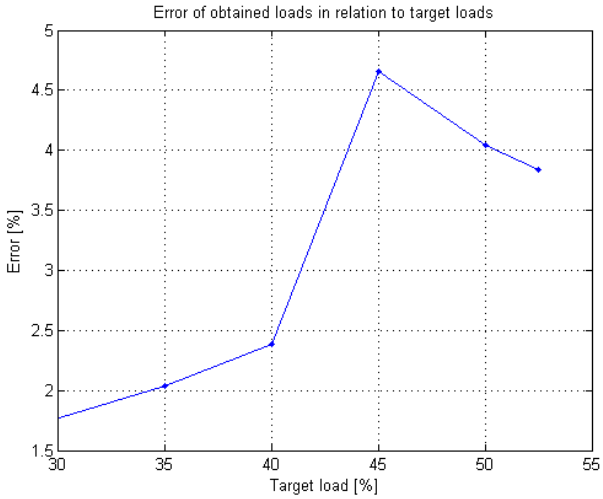

Figure 36. Loading error in each step for final test of blade 5.

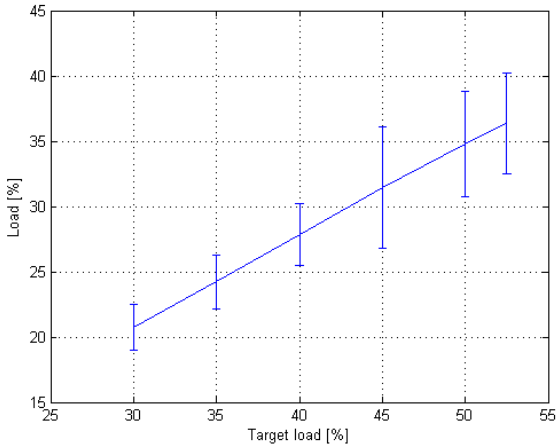

Figure 37. Loadings with error bars for each step for final test of blade 5.

3.4.4 Loading procedure comparison

Figure 38 and Figure 39 illustrate the time series of loading for blade test #3 and blade #4 which emphasise the differences of the individual loading schemes. Nevertheless, the measured displacement values can be used to compare the stiffness of the blades.

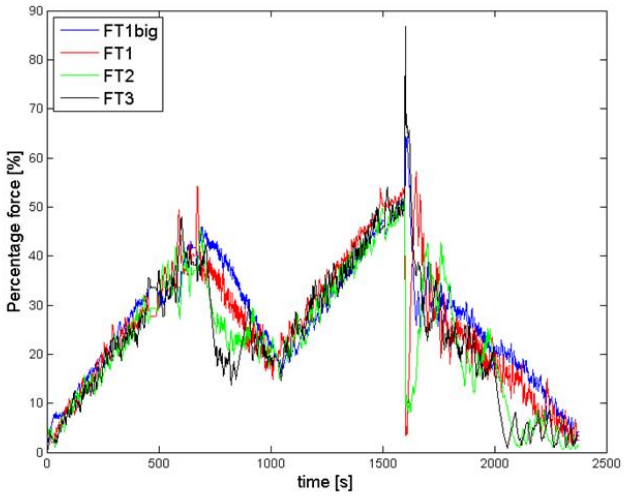

Figure 38. Time series of loading for blade 3 with four load application points.

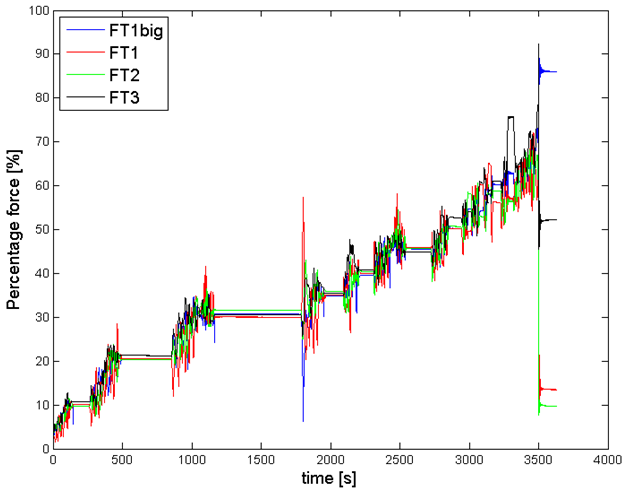

Figure 39. Time series of loading for blade 4 with four load application points.

3.5 Results and Discussion

In this section the measured values of different tests and blades are presented and compared. The presented results in this section are covering displacements and strains.

3.5.1 Deflections and stiffness comparison between blades 3, 4 and 5.

Figure 40 and Figure 41 present a comparison of the box girder deflection at 22 m and at 29 m between the blade #4 and #5. A linear behavior of the deflection as a function of the bending moment can be observed in both cases.

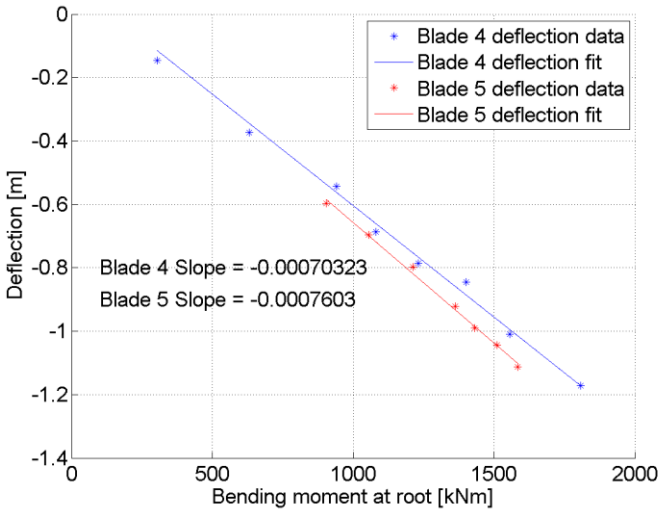

Figure 40. Comparison between deflection as a function of loads in blade 4 and 5 at 22m from root.

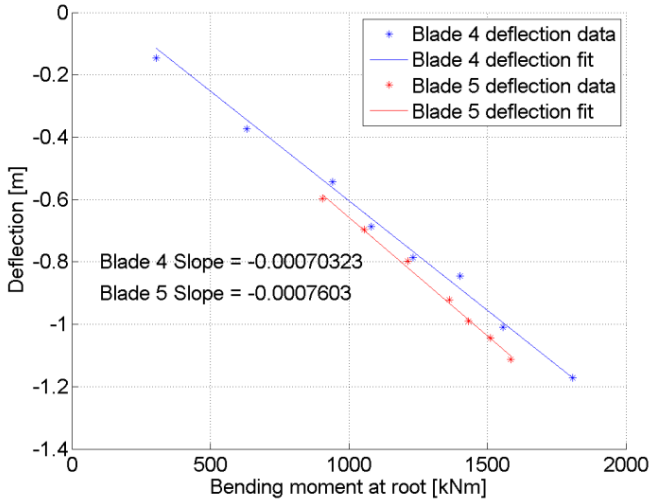

Figure 41. Comparison between deflection as a function of loads in blade #4 and #5 at 29m from root.

Figure 42 shows the box girder deflection at 16 m from the root and the trailing edge deflection at 13 and 16 m as a function of the load step. As expected in this case the deflection of two points with same distance from the root but one on trailing edge and one on the cap is not the same. A non-linear behaviour of the trailing edge deflection was detected after 40% load.

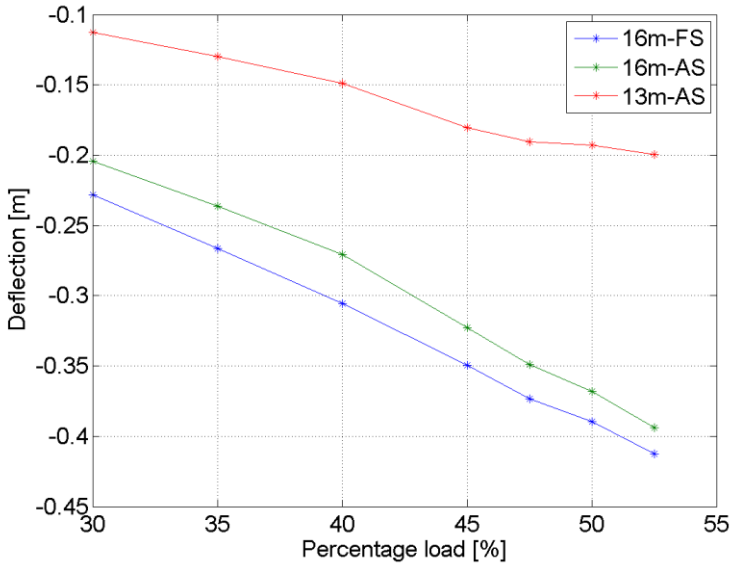

Figure 42. Comparison between the box girder deflection at 16 m from the root (16m-FS) and the trailing edge deflection at 13 (13m-AS) and 16 m. (16m-AS) for blade 5.

3.5.2 Strains on the trailing edge of blade 5, final test

Figure 43 presents the crucial points where electrical resistance strain gauges were installed on the blade airfoil.

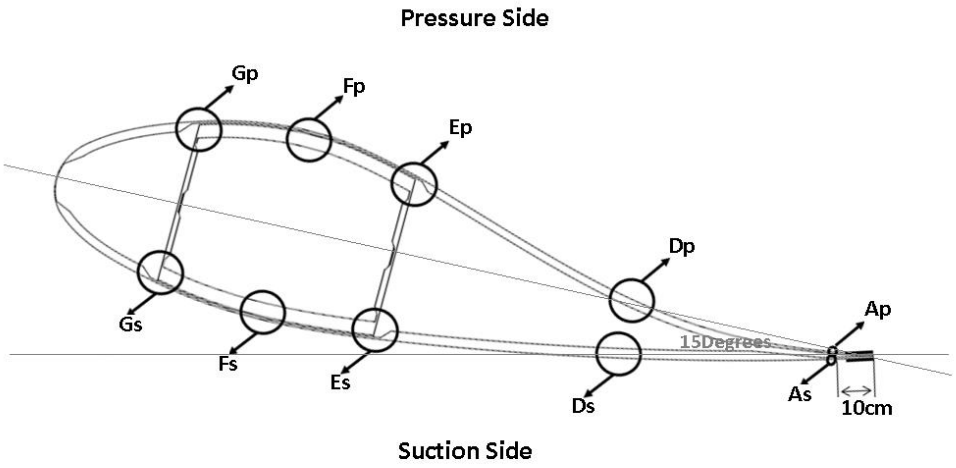

Figure 43. Strain values measured on the blade root through electrical resistance strain gauges

In Figure 44 the strains measured by the electrical resistance strain gauges at the blade root are shown as a function of time. The sensors are located on both the suction side and the pressure side of the blade, on the box girder (point F) and on the trailing edge pannel (point D).

Figure 45 present the strains measured by means of electrical resistance strain gauges on the trailing edge of the blade. In the plot it is obvious that all the points are under compression which is expected knowing that the blade has been mounted with 30 degrees pitch to investigate the buckling phenomena. Also, a strange behaviour can be seen in the time series of the sensors in 12.55 m and 12.70 m from the root. They do not follow the overall trend. This might be because of forming a buckling wave which will be investigated in the next report.

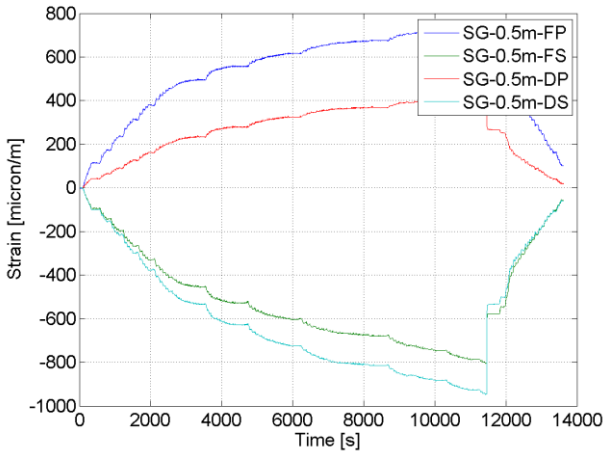

Figure 44. Strain values measured on the blade root through electrical resistance strain gauges.

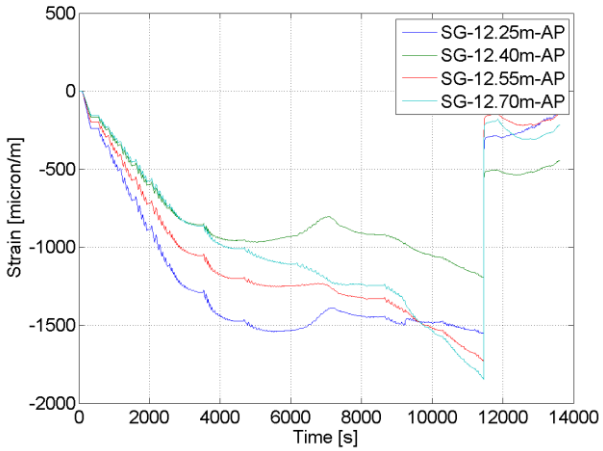

Figure 45. Strain values measured on the blade trailing edge through electrical resistance strain gauges.

The strain distribution measured along the blade trailing edge through the optic fiber system is presented in Figure 46, Figure 47 and Figure 48. Each of them is associated to a particular load value.

For an increasing load value, a non-linear behavior of the strain was detected.

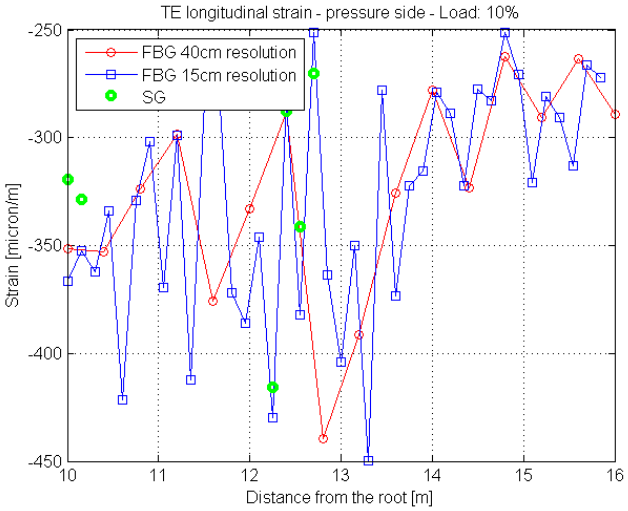

Figure 46. Comparison between strains measured on the two lines of FBG sensors at 10% load in pre-test 18.

.

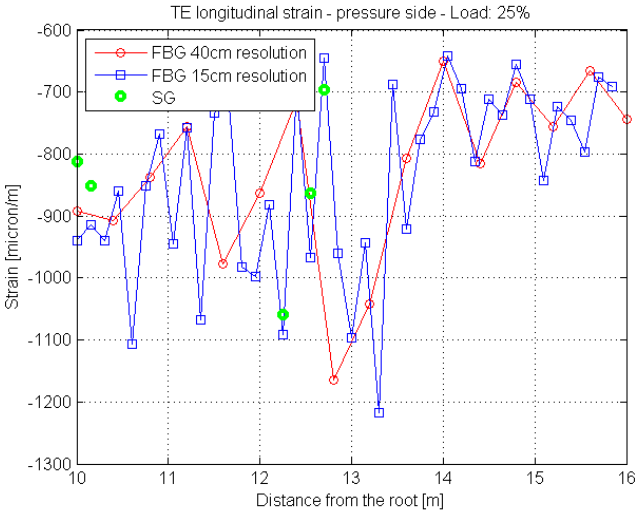

Figure 47. Comparison between strains measured on the two lines of FBG sensors at 25% load in pre-test 18.

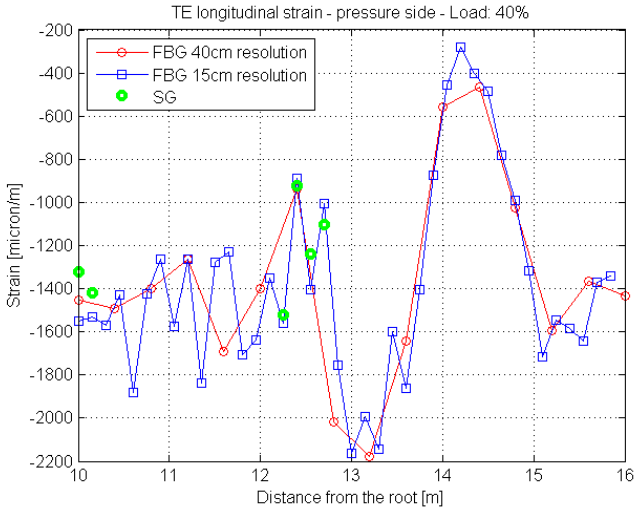

Figure 48. Comparison between strains measured on the two lines of FBG sensors at 40% load in pre-test 18.

3.6 Stereo photogrammetry results

3.6.1 Calibration

In Figure 49 the extracted corners on the calibration board are shown for image 1 and 2.

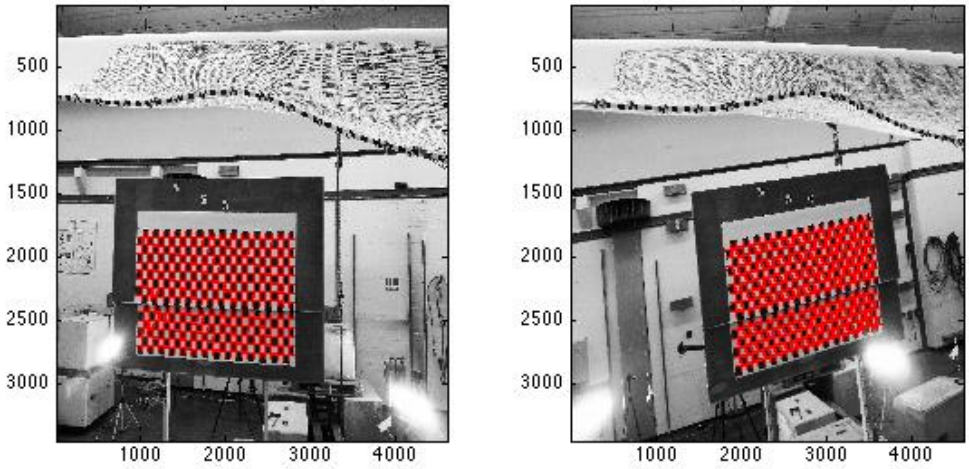

Figure 49. Extracted corners in the calibration are marked with red crosses.

In Figure 50 the absolute error of the calibration is plotted as a function of the in-plane coordinates for each of the three spatial directions. It can be seen that the order of error is less than one millimeter in the x-direction and the y-direction and larger in the out-of plane direction (z-direction). In the x- and y-directions, the error is somewhat shaped as a valley with larger errors at the borders of the calibration board. Especially in the upper right corner of the calibration board, the error in x-direction is large, and similarly along the right border of the calibration board, a larger error in y-direction is observed. These deviations might be caused by geometric imperfections of the calibration board or due to parts of the calibration board being slightly out of focus.

In Figure 51, histograms of the error in x-, y- and z-direction are shown. Each error histogram is fitted to a normal distribution f(εi) given by

$$f(\varepsilon i) = \frac{1}{\sigma\sqrt{2\pi}} exp\left[-\left(\frac{(\epsilon_i-\mu)^2}{2\sigma^2}\right)\right] \quad (13)$$

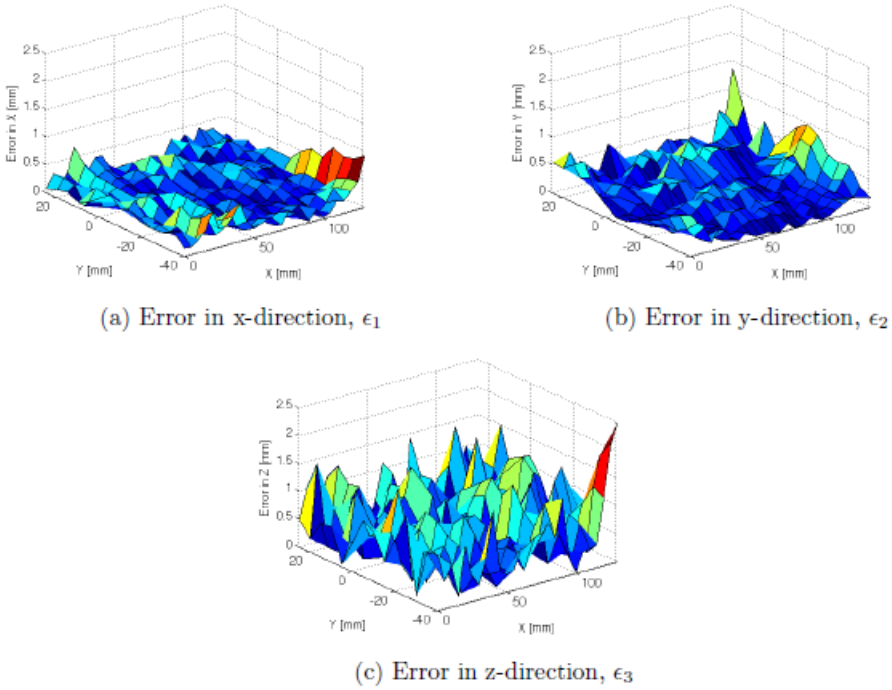

(a) Error in x-direction, ϵ_1 (b) Error in y-direction, ϵ_2

(c) Error in z-direction, ϵ_3

Figure 50. Absolute calibration error in x-, y- and z-direction

It can be seen that the error follows a normal distribution reasonably well. The error in all three directions is centered approximately around 0.0 which suggests that there is no significant systematic error in the corner prediction. Since the error seems to be normally distributed around 0, the standard deviation of the error is a reasonable measure of the uncertainty on the calibration. The uncertainty in each direction is therefore

$$\delta_x = 0.2\ mm$$
$$\delta_y = 0.3\ mm$$
$$\delta_z = 0.7\ mm$$

In order to compare the calibration to the one obtained by Shmueli et al. in a different calibration set-up, the mean and maximum of the absolute error are reported in Table 6 along with the values found by Shmueli et al.

Table 6 Calibration error.

calibration error	x	y	z
mean(ϵ_i), μ, [mm]	-0.01	-0.06	0.05
standard deviation, σ, [mm]	0.24	0.31	0.70
mean($\lvert\epsilon_i\rvert$), [mm]	0.19	0.25	0.57
max($\lvert\epsilon_i\rvert$), [mm]	0.93	1.35	2.49
mean($\lvert\epsilon_i\rvert$), [mm], Shmueli [3]	0.20	0.20	0.59
max($\lvert\epsilon_i\rvert$), [mm], Shmueli [3]	0.85	1.06	1.94

It can be seen that both the mean and the maximum correspond well between the two calibrations. However, the maximum error in the z-direction is larger in the calibration performed

in this report. The reason for the larger maximum calibration is perhaps due to a curved calibration board or that the one corner of the calibration board was slightly out of focus. The mean and maximum value of the absolute error are only included here in order to compare to the values obtained by Shmueli et al., since the standard deviation of the error is considered to be a better measure of the uncertainty than the mean of the absolute error. In any case, the standard deviation is larger, so this gives a more conservative value of the uncertainty.

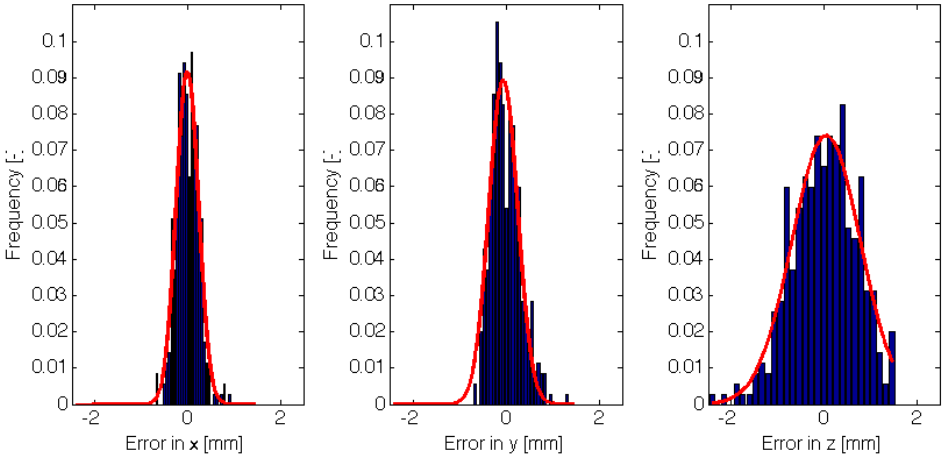

Figure 51. Distribution of the error on the calibration in each spatial direction, the red line *indicates a Gaussian fit with coefficient of determination R^2 as follows* ε_1 *:R2 = 0:922;* ε_2*:R2 = 0:90;* ε_3*: R2 = 0:915.*

3.6.2 Global displacement

The extracted pixel coordinates and the calibration matrix C described in the theory are used to determine the real world coordinates of the markers for each load case. The extracted pixel coordinates are shown in Figure 52 for an arbitrary set of images.

The distance manually measured between the markers can be used as a validation of the triangulation. In Figure 53, the difference between the real-world distance between markers and the triangulated distance is shown in a histogram along with a Gaussian fit. The number of bins in the histogram is seven which is considered a minimum reasonable number of data points to use for fitting. The coefficient of determination is R2 = 0:793 for the Gaussian fit. From looking at the histogram and the coefficient of determination it is seen that the distribution hardly follows a normal distribution. The difference between the distance found by the triangulation and the ideal distance is therefore not considered to be random and the uncertainty is not given as the standard deviation.

The difference in distance is between -2.7 mm and 6.0mm where the largest difference is between the markers at 15.95m and 15.75m. It is expected that the computed coordinates of the marker at 15.95m and 12.95m are determined with a smaller precision than the remaining markers. This is due to the presence of the nail and wire of the ASM on top of the marker which makes it difficult for the corner prediction method to determine the centre of the marker. Excluding these distances, the largest error is less than 2mm. The uncertainty on the computed distance is determined by the error on the calibration, whereas the uncertainty on the real-world

distance between the markers is at least 1 mm in each direction, since the markers are positioned manually. It is expected that the uncertainty in the position of the markers is the major reason for the difference. The computed distance between the markers is therefore reasonably close to the expected distance and this shows that the real world coordinates are reliable.

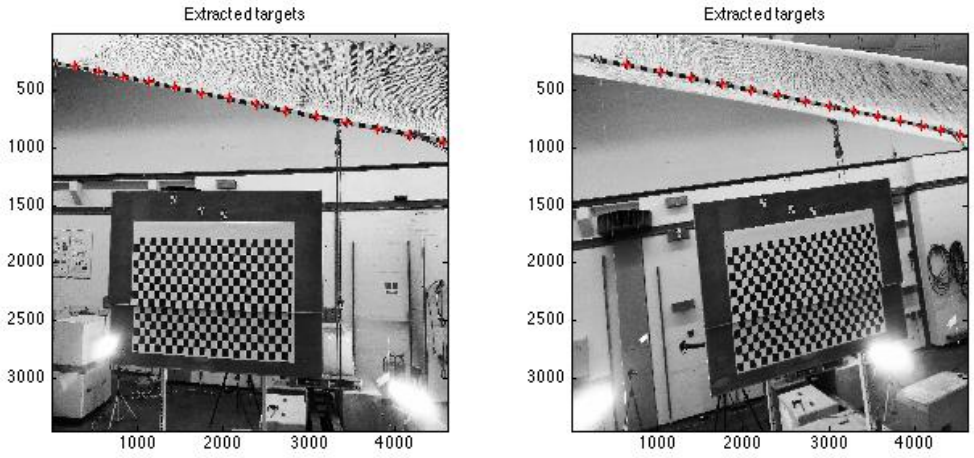

Figure 52. Extracted pixel coordinates of the markers on the unloaded blade are marked with red crosses.

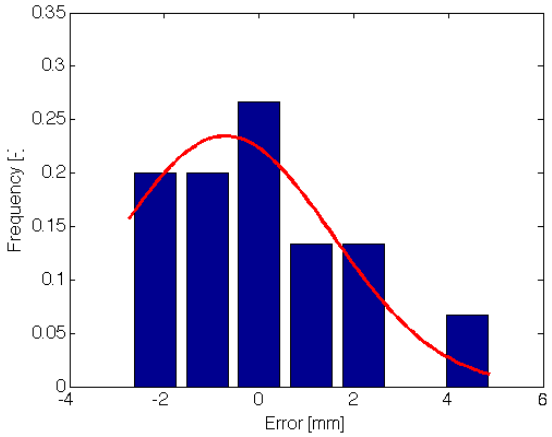

Figure 53. Histogram of error in the obtained distance between the markers.

The global displacement of the markers has been computed from the real world coordinates obtained from the stereo photogrammetry. In Figure 54, the global displacement is plotted as a function of distance from the root r for all the load cases. At the lower loads 30% and 35%, the displacement is nearly linear, however, as the load increases, a buckle appears with its peak located at around 14 m from the root. At r = 12:95m, the displacement seems to be slightly off compared to the neighboring distances r = 12:75m and r = 13:0m. The uncertainty on the real world coordinates of the markers in 12.95m and 15.95m is larger than the uncertainty on the remaining markers, due to the presence of the ASM. In Appendix A, close-up images of the marker and ASM in r = 12:95m and r = 15:95m are provided. Therefore, a better value of the displacement at this point might be to take a linear interpolation between the two neighboring

points. The displacement at r = 12:95m is important since we want to compare the displacement obtained by the stereo-photogrammetry method to the displacement measured by the ASM. In order to make a reasonable comparison it is crucial to compare the displacement in the same distance r from the root. Ideally, a linear interpolation between r = 15:75m and r = 16:0m should be made as well to check if the results compare better, but the marker at 16m is not captured in both images, and therefore a linear interpolation is not possible. The stereo photogrammetry displacement in r = 15:95 is therefore best compared to the ASM by taking the displacement of the marker.

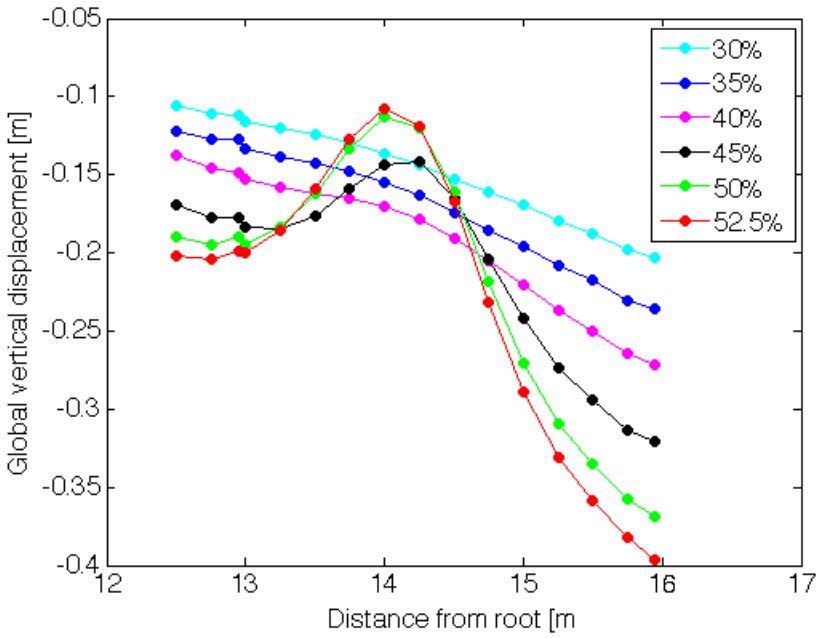

Figure 54. Global displacement in the vertical direction as a function of distance from the root.

In Figure 55, the vertical displacement measured by the ASM is plotted on top of the SDMS results. The displacements measured by the ASM seem to be in good correspondence with the SDMS results, especially at r = 15:95m. In Figure 56, the measured displacement obtained by ASM and SDMS is plotted as a function of load ratio at r = 12:95m and r = 15:95m. The interpolated displacement at r = 12:95m is presented as well to compare if the direct measurement or the interpolated displacement. It is seen that the displacement obtained by the stereo photogrammetry and the ASM have a high degree of agreement. Especially at r = 15:95m, the two measurements overlap strongly. In r = 12:95m, the measurements correspond well, however the overlap is not as strong as in r = 15:95m.

It is hard to say whether the displacement of the marker or the interpolated displacement gives a better correspondence to the ASM measurement. There seems to be a systematic error where the linear interpolation is used, since the displacement is around 2mm off in each load case. The displacement obtained from the marker directly has a larger uncertainty, due to the presence of the ASM. The difference between the ASM and the stereo photogrammetry results is between 0.5% and 2.0% for the direct marker at 12.95m, it is between 0.05% and 0.8% for

the marker at 15.95m and between 0.6% and 2.0% for the interpolated displacement at r=12.95m.

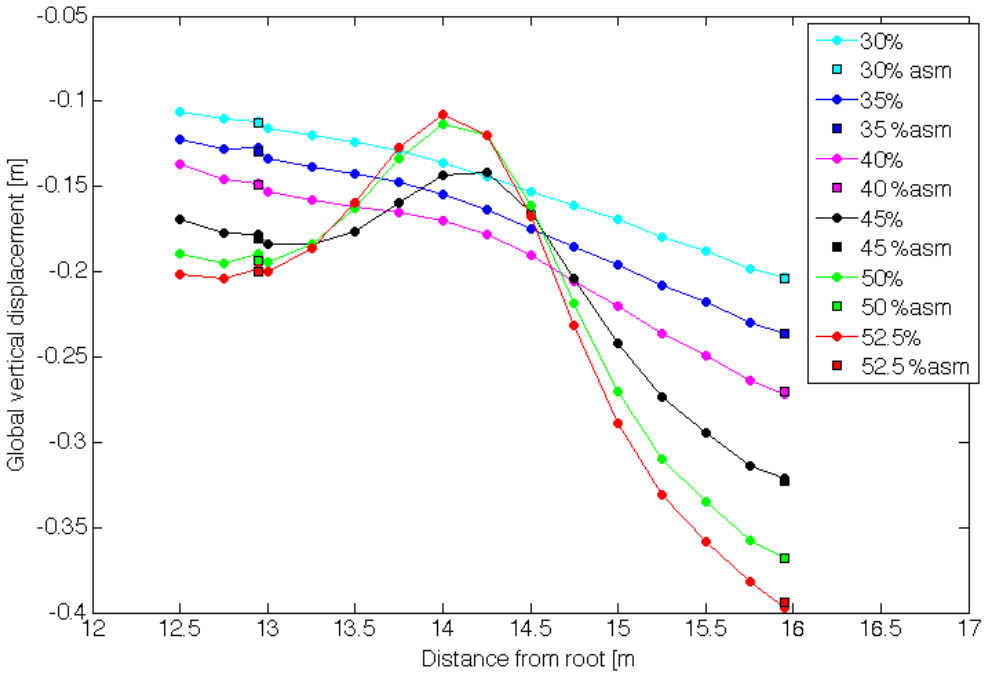

Figure 55. Vertical displacement as a function of distance from the root, comparison of SDMS results and ASM results.

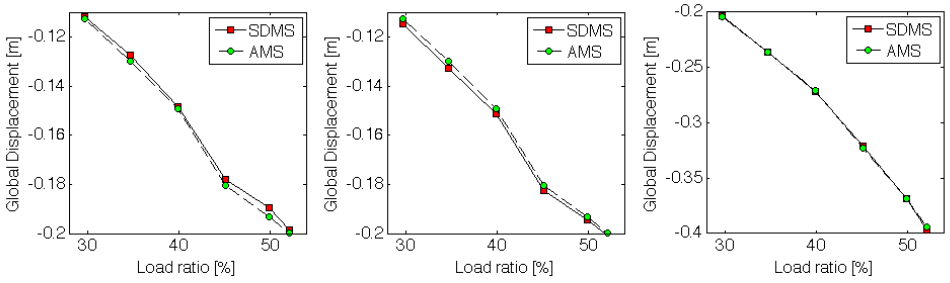

Figure 56. Vertical displacement along trailing edge obtained via SDMS and ASM at 13m marker and 16m marker. left) marker in r =12.95m, center) linear interpolation between 12.75m and 13.00m, right) marker in 15.95m

References

[1] Nielsen P.H., Berring P., Pavese C. and Branner K. (2013). Rotor blade full-scale fatigue testing technology and research, DTU Wind Energy E-0041, Department of Wind Energy, Technical University of Denmark

[2] L.A.G. Seabra (2004). Life time equivalent fatigue load analysis of a SSP 34m blade, DTU Wind Energy Report-1, Department of Wind Energy, Technical University of Denmark

[3] Amzallag C, Gerey JP, Robert JL, Bahuaud J (1994). Standardization of the rainflow counting method for fatigue analysis. Int J Fatigue 1994;16:287–93

[4] IEC Standard 61400-23 rev L (2011): Full-scale structural testing of rotor blades, International Electrotechnical Commission

[5] Miner M.A. (1945). Cumulative damage in fatigue. J Appl Mech, 12, A64-A159

[6] Shmueli J., Eder M.A. and Tesauro A. (2015). A versatile stereo photogrammetry based technique for measuring fracture mode displacements in structures, Precision Engineering, 39, pp38-46.

[7] C. Harris, M. Stephens, A combined corner and edge detector, Proc. of fourth alvey vision conference, 1998, p 147-151

[8] ISO/IEC Guide 98-3:2008. Uncertainty of measurement -- Part 3: Guide to the expression of uncertainty in measurement (GUM:1995)

Acknowledgements

This work is supported by a grant of the Sino-Danish Renewable Energy Development (RED) Programme Component 2. The supported RED-project is titled “Wind Turbine Rotor Blade Testing Technology Research and Platform Construction” and is entered by and between the Royal Danish Embassy in Beijing, Baoding Diangu Renewable Energy Testing and Research Co. Ltd. and DTU Wind Energy. Danida file reference number is 104.Kina.1.MFS.4-1-2-5. The support is gratefully acknowledged.

Martin Alexander Eder is gratefully acknowledged for being test leader on the full-scale tests where the Fiber Bragg sensors and stereo photogrammetry system were applied.

Malene Louise Hovgaard Vested and Amin Ghadirian have been student workers and have helped with performing the measurements, helped with date analysis and calculations and drafted part of the text. Their work is gratefully acknowledged.

Appendix A

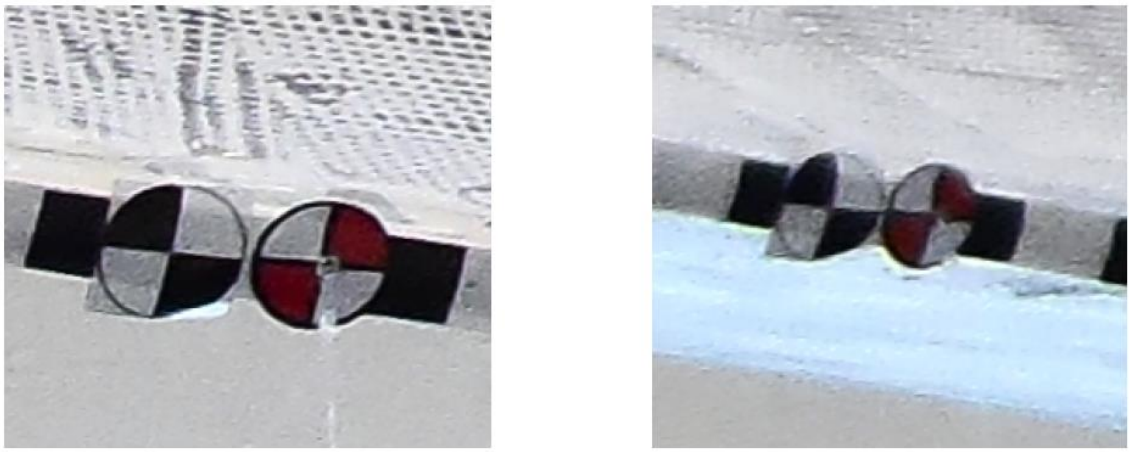

(a) Image 1 (b) Image 2

Figure A-1 The red marker is positioned at 12.95m, note that the ASM is visible on the red marker as a nail and a wire

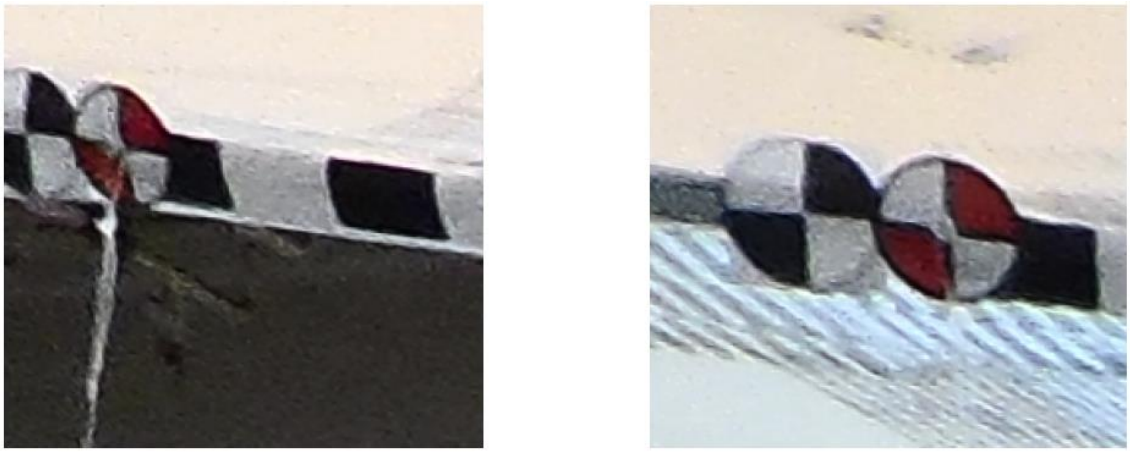

(a) Image 1 (b) Image 2

Figure A-2 The red marker is positioned at 15.95m, note that the ASM is visible on the red marker as a nail and a wire

DTU Wind Energy is a department of the Technical University of Denmark with a unique integration of research, education, innovation and public/private sector consulting in the field of wind energy. Our activities develop new opportunities and technology for the global and Danish exploitation of wind energy. Research focuses on key technical-scientific fields, which are central for the development, innovation and use of wind energy and provides the basis for advanced education at the education.

We have more than 240 staff members of which approximately 60 are PhD students. Research is conducted within nine research programmes organized into three main topics: Wind energy systems, Wind turbine technology and Basics for wind energy.

Technical University of Denmark
Department of Wind Energy
Frederiksborgvej 399
Building 118
4000 Roskilde
Denmark
Telephone 46 77 50 85

info@vindenergi.dtu.dk
www.vindenergi.dtu.dk